Interfacial states and far-from-equilibrium transitions in the epitaxial growth and erosion on (110) crystal surfaces

Artem Levandovsky,[1,*] Leonardo Golubović,[1] and Dorel Moldovan[2]
[1]*Department of Physics, West Virginia University, Morgantown, West Virginia 26506-6315, USA*
[2]*Mechanical Engineering Department, Louisiana State University, Baton Rouge, Louisiana 70803-6413, USA*
(Received 9 August 2004; revised manuscript received 24 October 2006; published 1 December 2006)

We discuss the far-from-equilibrium interfacial phenomena occurring in the multilayer homoepitaxial growth and erosion on (110) crystal surfaces. Experimentally, these rectangular symmetry surfaces exhibit a multitude of interesting nonequilibrium interfacial structures, such as the rippled one-dimensional periodic states that are not present in the homoepitaxial growth and erosion on the high symmetry (100) and (111) crystal surfaces. Within a unified phenomenological model, we reveal and elucidate this multitude of states on (110) surfaces as well as the transitions between them. By analytic arguments and numerical simulations, we address experimentally observed transitions between two types of rippled states on (110) surfaces. We discuss several intermediary interface states intervening, via consecutive transitions, between the two rippled states. One of them is the rhomboidal pyramid state, theoretically predicted by Golubovic *et al.* [Phys. Rev. Lett. **89**, 266104 (2002)] and subsequently seen, by de Mongeot and co-workers, in the epitaxial erosion of Cu(110) and Rh(110) surfaces [A. Molle *et al.*, Phys. Rev. Lett. **93**, 256103 (2004), and A. Molle *et al.*, Phys. Rev. B **73**, 155418 (2006)]. In addition, we find a number of interesting intermediary states having structural properties somewhere between those of rippled and pyramidal states. Prominent among them are the rectangular rippled states of long rooflike objects (huts) recently seen on Ag(110) surface. We also predict the existence of a striking interfacial structure that carries nonzero, persistent surface currents. Periodic surface currents vortex lattice formed in this so-called buckled rippled interface state is a far-from-equilibrium relative of the self-organized convective flow patterns in hydrodynamic systems. We discuss the coarsening growth of the multitude of the interfacial states on (110) crystal surfaces.

DOI: 10.1103/PhysRevE.74.061601 PACS number(s): 81.15.Aa, 89.75.Kd, 05.90.+m

I. INTRODUCTION

Mutilayer epitaxial growth and erosion of crystal surfaces often exhibits the formation of fascinating surface nanostructures [1–10]. At their origin is the classical Ehrilich-Schwoebel-Villain instability [5,6]. Thus, on high symmetry (100) and (111) surfaces, pyramidal structures are frequently seen in the homoepitaxial deposition growth and erosion, which is essentially a deposition of surface vacancies by ion beams [7]. These pyramids grow in time via far-from-equilibrium coarsening processes studied in numerous experiments and simulations on high symmetry crystal surfaces, such as the square symmetry (100) surfaces and the hexagonal symmetry (111) surfaces [1–4,7,8,12]. However, much less is known about related growth phenomena on low symmetry surfaces. Thus, the far-from-equilibrium interfacial structures formed in the epitaxial growth and erosion on rather typical *rectangular* symmetry (110) crystal surfaces have attracted attention only recently [9,10]. Rather than pyramids, rippled one-dimensional (1D) (nearly) periodic structures are more commonly seen on these surfaces, such as Fe(110) [11], Ag(110) [9,10], Cu(110) and Rh(110) [13]. There are two types of these rippled states, with their wave vectors oriented along the two perpendicular principal axes of the (110) surfaces. In addition to the rippled states, intriguing *intermediary states* of interface have been recently revealed in the "90° ripple rotation" transitions between the two types of rippled states on Ag (110) surfaces [9,10], and, more recently, on Cu(110) and Rh(110) surfaces [13]. These intermediary states are believed to have a pyramidal character. Most recently, exotic pyramidal structures have been seen also on Al(110), having the form of self-assembled "huts," i.e., rooflike pyramids [14].

In this study, we discuss these far-from-equilibrium phenomena occurring in the multilayer epitaxial growth and erosion on (110) surfaces. To elucidate the interfacial structures growing on these low symmetry crystal surfaces, we present detailed exposition of the theory briefly outlined before in our letter [3]. Within a unified phenomenological model derived in Sec. II, we expose a generic multitude of interfacial states on (110) surfaces as well as the far-from-equilibrium phase transitions between these states. By analytic arguments and numerical simulations, we investigate the generic nonequilibrium phase diagram of (110) surfaces. In particular, we address the experimentally observed transitions and intermediary states between the two aforementioned types of rippled states. We predict and discuss a number of intermediary interface states intervening, via consecutive transitions, between the two rippled states (Secs. III and IV). One of them is the rhomboidal pyramid state that has been theoretically predicted by us in Ref. [3] and subsequently seen by de Mongeot and co-workers in the epitaxial erosion of Cu(110) and Rh(110) surfaces [13]. In addition, our model yields a number of experimentally interesting intermediary states having structural properties somewhere between those of rippled and pyramidal states (Secs. III and IV). Among them

*Present address: Department of Chemical and Petroleum Engineering, University of Pittsburgh, Pittsburgh, PA 15261, USA.

are two rectangular rippled states of long rooflike objects (huts). These states, theoretically anticipated by us in Ref. [3], represent the long time-scale form of the aforementioned rooflike pyramid (huts) state more recently revealed to emerge in the epitaxial growth on Al(110) [14]. In fact, our basic rectangular rippled structure [the checkerboard arrangements of huts and pits (inverted huts)] has been clearly seen in the ion erosion experiments on Ag(110) [see Ref. [10] and Fig. 4(d) therein]. We predict that there are two types of the rectangular rippled states, with their wave vectors oriented along the two perpendicular principal axes of the (110) surfaces. To elucidate the transition between these states, we generalize the classical Gibbs phase coexistence rule to the situations involving far-from-equilibrium phase transitions, in the absence of an effective free energy governing dynamics (Secs. III and IV, and Appendix B). Our theory [3] has revealed also the exotic buckled rippled interface state, discussed here in detail. Unlike the usual interfacial states (see, e.g., Refs. [1,2,5] and references therein), the interfaces in the buckled rippled state exhibit nonvanishing, persistent surface currents forming a periodic convectionlike pattern of vortices (Sec. IV). This interface state is a far-from-equilibrium relative of the Rayleigh-Benard's and other self-organized convective flow patterns occurring in hydrodynamic systems. We discuss the dynamics of various interfacial states on (100) surfaces (Sec. IV). The coarsening, i.e., the growth of the spatial period of the rippled states on (110) surfaces is shown to be mediated by ensembles of climbing dislocations destroying perfect periodicity of these states. In Sec. IV we also discuss the interfacial phenomena underlying the experimentally observed enhanced coarsening of the rhomboidal pyramid state intervening between the two rippled states [13].

The layout of this paper is as follows: In Sec. II, we derive our unified phenomenological model for multilayer epitaxial growth and erosion on (110) surfaces. In Sec. III, we derive the kinetic phase diagram of the model exhibiting generic multitude of growing interfacial states on (110) surfaces. In Sec. IV, we discuss the structure and coarsening dynamics of these states, as well as the related experiments on Cu(110) and Rh(110) surfaces. Appendix A outlines facet stability analysis underlying the Sec. III discussions. In Appendix B we prove the Sec. III theorem generalizing the classical Gibbs phase coexistence rule to the situations involving the far-from-equilibrium phase transitions studied here.

II. RECTANGULAR SYMMETRY AND INTERFACE DYNAMICS

Here, we introduce a continuum model for the epitaxial growth and erosion on (110) crystal surfaces. We base our discussion on the general phenomenological approach to multilayer epitaxial growth in the absence of (typically weak) adatom desorption and vacancy creation [5,6]. Under these conditions, the deposited film volume is conserved and the height function $h(\vec{x},t)$ describing interface shape must obey this conservation law. In the frame comoving with the interface, the interface velocity $\partial h/\partial t$ can be thus represented as a divergence of the surface current $\vec{J}=(J_1,J_2)$,

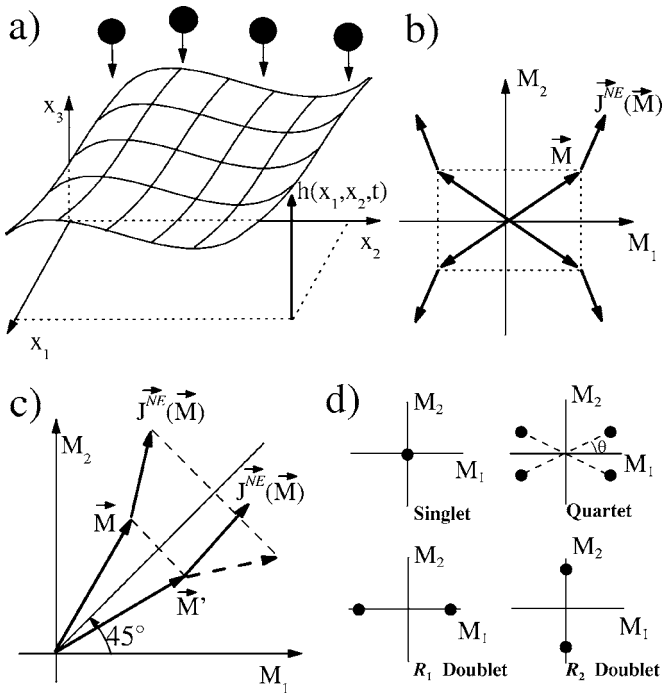

FIG. 1. (a) The growing interface geometry. (b) Transformations of the surface nonequilibrium current vector $\vec{J}^{NE}(\vec{M})$ under the symmetry operations of the (110) surface. (c) The absence of the diagonal reflection symmetry on (110) surfaces: The slope vectors $\vec{M}$ and $\vec{M}'$ here are related by diagonal reflection. However, the corresponding current vectors $\vec{J}^{NE}(\vec{M})$ and $\vec{J}^{NE}(\vec{M}')$ are not related by the diagonal reflection. (d) Four types of zeros of the $\vec{J}^{NE}(\vec{M})$ on (110) surfaces: singlet, quartet, and two types of doublets.

$$\frac{\partial h(\vec{x},t)}{\partial t} = -\vec{\nabla}\cdot\vec{J} = -\frac{\partial J_1}{\partial x_1} - \frac{\partial J_2}{\partial x_2}. \tag{2.1}$$

Here $\vec{x}=(x_1,x_2)$ is two-dimensional (2D) base plane vector [Fig. 1(a)]. Due to the vertical translation symmetry $h\to h+\text{const}$, the surface current can depend only on spatial derivatives of $h(x_1,x_2,t)$. It is convenient to express $\vec{J}$ in the form

$$\vec{J} = \vec{J}^{NE}(\vec{\nabla}h) + \vec{J}^{curv}. \tag{2.2}$$

Here, the first term is the surface nonequilibrium current $\vec{J}^{NE}(\vec{M})$, which is a function of the local interface slope vector $\vec{M}=\vec{\nabla}h=(M_1,M_2)$ [5], see Fig. 1(b). $\vec{J}^{curv}$ in Eq. (2.2) is the surface curvature current. This current depends on higher order spatial derivatives of h and vanishes on a flat surface (facet). For example, for an isotropic surface, $\vec{J}^{curv}$ contains a term isomorphic to the Mullins surface diffusion current $\propto -\vec{\nabla}(\nabla^2 h)$, contributing to the interface velocity in Eq. (2.1) the term $-\kappa(\nabla^2)^2 h$. For the rectangular symmety surfaces, this contribution to Eq. (2.1) has the more general form

$$-\vec{\nabla}\vec{J}^{SD} = -\kappa_{11}\left(\frac{\partial}{\partial x_1}\right)^4 h - 2\kappa_{12}\left(\frac{\partial}{\partial x_1}\right)^2\left(\frac{\partial}{\partial x_2}\right)^2 h - \kappa_{22}\left(\frac{\partial}{\partial x_2}\right)^4 h. \tag{2.3}$$

Note that for isotropic surfaces, $\kappa_{11}=\kappa_{12}=\kappa_{22}=\kappa$, whereas for square symmetry (001) surfaces, $\kappa_{11}=\kappa_{22}\neq\kappa_{12}$. (110) surfaces have the natural coordinate system (x_1,x_2) associated with the principal axes parallel to the sides of the surface rectangular unit cell. This coordinate system is already assumed in Eq. (2.3) as well as in the following. Rectangular symmetry of (110) involves two major symmetry operations, which are the reflections across the principal axis of (110) surface, $\Re_1:(x_1,x_2)\to(-x_1,x_2)$, and $\Re_2:(x_1,x_2)\to(x_1,-x_2)$. As $M_1=\partial h/\partial x_1$ and $M_2=\partial h/\partial x_2$, under $\Re_1$,

$$\Re_1:(M_1,M_2)\to(-M_1,M_2), \tag{2.4}$$

while under $\Re_2$,

$$\Re_2:(M_1,M_2)\to(M_1,-M_2). \tag{2.5}$$

The rectangular symmetry of (110) imposes a few ubiquitous properties of the nonequilibrium current $\vec{J}^{NE}(\vec{M})=[J_1^{NE}(M_1,M_2),J_2^{NE}(M_1,M_2)]$. This vector must transform in the *same* way the slope vector $\vec{M}=(M_1,M_2)$ transforms under the transformations leaving the (110) surface invariant. In other words, for any surface symmetry operation S,

$$\vec{J}^{NE}(S\vec{M})=S\vec{J}^{NE}(\vec{M}), \tag{2.6}$$

see Fig. 1(b). Thus, under $\Re_1$,

$$J_1^{NE}(-M_1,M_2)=-J_1^{NE}(M_1,M_2),$$

$$J_2^{NE}(-M_1,M_2)=J_2^{NE}(M_1,M_2), \tag{2.7}$$

while under $\Re_2$, by Eq. (2.5),

$$J_1^{NE}(M_1,-M_2)=J_1^{NE}(M_1,M_2),$$

$$J_2^{NE}(M_1,-M_2)=-J_2^{NE}(M_1,M_2). \tag{2.8}$$

Under the inversion symmetry of (110), $Inv=\Re_1\otimes\Re_2$, one has $Inv:(x_1,x_2)\to(-x_1,-x_2)$ implying $Inv:(M_1,M_2)\to(-M_1,-M_2)$. Thus,

$$\vec{J}^{NE}(-\vec{M})=-\vec{J}^{NE}(+\vec{M}). \tag{2.9}$$

We stress that the rectangular summetry (110) surfaces do *not* have invariance under the *diagonal reflection*, $\Re_{diag}:(x_1,x_2)\to(x_2,x_1)$, i.e., $(M_1,M_2)\to(M_2,M_1)$. Thus, on rectangular symmetry surfaces, in general,

$$\vec{J}^{NE}(M_1,M_2)\neq\vec{J}^{NE}(M_2,M_1), \tag{2.10}$$

because the two principal axis of (110) are *not* equivalent to each other; see Fig 1(c). In this respect, (110) surfaces are different from the square symmetry (001) surfaces for which Eq. (2.10) holds with equality [1,2,4]. Commonly, stable zeros of the nonequilibrium current, solving the equation $\vec{J}^{NE}(\vec{M})=\vec{0}$, correspond to the preferred slopes $\vec{M}$ of the facets that develop across the growing interface and organize themselves into large structures, e.g., the square pyramids on (100) surfaces [1–4]. Importantly, by Eq. (2.6), if $\vec{M}$ is a zero of $\vec{J}^{NE}$, then $S\vec{M}$ is also a zero of $\vec{J}^{NE}$, where S is any surface symmetry operation. For (110) surfaces, $S=(\Re_1,\Re_2,Inv)$ and one can see that there are *four* possible types of these preferred slope vectors depicted in Fig. 1(d): (i) *Singlet*, for which *both* slope components vanish, $M_1=M_2=0$. (ii) *Doublets* of two equivalent (symmetry related) slope vectors, for which *one* of the two components of the slope vector vanishes. There are *two* types of doublets: the pair $(\pm M_1,0)$ and the pair $(0,\pm M_2)$, called, respectively, as R_1 and R_2 doublet in Fig. 1(d). Importantly for the following, these two types of doublets are *not* equivalent to each other. The diagonal reflection, R_{diag}, that would relate them is not a symmetry of (110) surface; see Eq. (2.10). (iii) *Quartet* of four equivalent slope vectors, for which *none* of the slope components vanishes, $(\pm M_1,\pm M_2)$, see Fig 1(d). In the unstable epitaxial growth, the singlet at $\vec{M}=0$ is unstable, and stable facets may thus correspond to the doublets or to the quartet; see Sec. III.

We will expose the phenomenology of the epitaxial growth and erosion on (110) surfaces, by considering the dynamical model Eq. (2.1) with generic form of the nonequilibrium current $\vec{J}^{NE}(\vec{M})$. It can be represented as an expansion in powers of $\vec{M}$ respecting the restrictions imposed by the rectangular symmetry. Thus, by the inversion symmetry of (110) in Eq. (2.9), this expansion must contain only odd powers of $\vec{M}$. Furthermore, by respecting the reflection symmetries in Eqs. (2.7) and (2.8), we arrive at the general expansion of the form,

$$J_1^{NE}(M_1,M_2)=M_1[r_1-u_{11}M_1^2-u_{12}M_2^2+\cdots],$$

$$J_2^{NE}(M_1,M_2)=M_2[r_2-u_{22}M_2^2-u_{21}M_1^2+\cdots]. \tag{2.11}$$

By considering typical situations with small selected slopes, the simplest basic model is naturally obtained by truncating out the higher order terms in the ellipses in Eq. (2.11). We stress that in the expression for the $\vec{J}^{NE}(\vec{M})$ in Eq. (2.11), one has $r_1\neq r_2$, $u_{12}\neq u_{21}$, and $u_{11}\neq u_{22}$ in general for (110) surfaces due to their diagonal asymmetry, Eq. (2.10). This is in contrast to the square symmetry (100) surfaces that have diagonal symmetry, $\vec{J}^{NE}(M_1,M_2)=\vec{J}^{NE}(M_2,M_1)$, implying $r_1=r_2$, $u_{12}=u_{21}$, and $u_{11}=u_{22}$.

For the special case $u_{12}=u_{21}=u$, the $\vec{J}^{NE}(\vec{M})$ Eq. (2.11) becomes a gradient of a potential,

$$\vec{J}^{NE}(\vec{M})=-\frac{\partial U(\vec{M})}{\partial\vec{M}}, \tag{2.12a}$$

with the potential

$$U(\vec{M})=-\frac{r_1}{2}M_1^2-\frac{r_2}{2}M_2^2+\frac{u_{11}}{4}M_1^4+\frac{u}{2}M_1^2M_2^2+\frac{u_{22}}{4}M_2^4, \tag{2.12b}$$

whereas the interface dynamics equation (2.1) can be shown to be equivalent to

$$\frac{\partial h(x,t)}{\partial t}=-\frac{\delta F_{eff}}{\delta h(x,t)}. \tag{2.13a}$$

Here, F_{eff} is an effective free energy functional of the form $F_{eff}(h)=F_{SD}+F_{NE}$, with

$$F_{NE} = \int d^2x U(\vec{M}) \tag{2.13b}$$

and

$$F_{SD} = \int d^2x \left[\frac{\kappa_{11}}{2}\left(\frac{\partial^2 h}{\partial x_1^2}\right)^2 + \frac{\kappa_{12}}{2}\left(\frac{\partial^2 h}{\partial x_1 \partial x_2}\right)^2 + \frac{\kappa_{22}}{2}\left(\frac{\partial^2 h}{\partial x_2^2}\right)^2 \right]. \tag{2.13c}$$

We stress that for $u_{12} \neq u_{21}$ there is *no* F_{eff} that would generate dynamics via Eq. (2.13a). In the following, we disscuss, both analiticaly and numericaly, the general case with $u_{12} \neq u_{21}$, as implied by diagonal asymmetry Eq. (2.10). By Eqs. (2.1)–(2.3) and (2.11), we obtain the full kinetic model,

$$\begin{aligned}\frac{\partial h}{\partial t} = &- \frac{\partial}{\partial x_1}\left\{ \frac{\partial h}{\partial x_1}\left[r_1 - u_{11}\left(\frac{\partial h}{\partial x_1}\right)^2 - u_{12}\left(\frac{\partial h}{\partial x_2}\right)^2 \right] \right\} \\ &- \frac{\partial}{\partial x_2}\left\{ \frac{\partial h}{\partial x_2}\left[r_2 - u_{22}\left(\frac{\partial h}{\partial x_2}\right)^2 - u_{21}\left(\frac{\partial h}{\partial x_1}\right)^2 \right] \right\} \\ &- \kappa_{11}\left(\frac{\partial}{\partial x_1}\right)^4 h - 2\kappa_{12}\left(\frac{\partial}{\partial x_1}\right)^2\left(\frac{\partial}{\partial x_2}\right)^2 h - \kappa_{22}\left(\frac{\partial}{\partial x_2}\right)^4 h.\end{aligned} \tag{2.14}$$

The model in Eq. (2.14) depends on six major parameters of the nonequilibrium current $\vec{J}^{NE}(\vec{M})$, Eq. (2.10): r_1, r_2, u_{11}, u_{22}, u_{12}, and u_{21}. Importantly, this number can be reduced to only three independent parameters by applying to the model Eq. (2.14) the *anisotropic* rescaling,

$$h = Hh', \quad x_1 = X_1 x_1', \quad x_2 = X_2 x_2', \quad t = Tt', \tag{2.15}$$

with suitably chosen rescaling coefficients H, T, X_1, and X_2. By choosing them as

$$H = T = \frac{1}{4}\left(\frac{r_1}{\sqrt{u_{11}}} + \frac{r_2}{\sqrt{u_{22}}}\right)^2,$$

$$X_1 = H^{3/4} {u_{11}}^{1/4}, \quad X_2 = H^{3/4} {u_{22}}^{1/4}, \tag{2.16}$$

the model in Eq. (2.14) assumes the form

$$\begin{aligned}\frac{\partial h'}{\partial t'} = &- \frac{\partial}{\partial x_1'} J_1' - \frac{\partial}{\partial x_2'} J_2' - k_{11}\left(\frac{\partial}{\partial x_1'}\right)^4 h' \\ &- 2k_{12}\left(\frac{\partial}{\partial x_1'}\right)^2\left(\frac{\partial}{\partial x_2'}\right)^2 h' - k_{22}\left(\frac{\partial}{\partial x_2'}\right)^4 h',\end{aligned} \tag{2.17a}$$

with $k_{11} = (H/X_1^4)\kappa_{11}$, $k_{12} = (H/X_1^2 X_2^2)\kappa_{12}$, $k_{22} = (H/X_2^4)\kappa_{22}$, and,

$$\begin{aligned}J_1' &= M_1'[1 + a - {M_1'}^2 - (b + c){M_2'}^2], \\ J_2' &= M_2'[1 - a - {M_2'}^2 - (b - c){M_1'}^2].\end{aligned} \tag{2.17b}$$

Here, $M_1' = \partial h'/\partial x_1'$ and $M_2' = \partial h'/\partial x_2'$, whereas a, b, and c are the three independent dimensionless parameters

$$a = \frac{r_1/\sqrt{u_{11}} - r_2/\sqrt{u_{22}}}{r_1/\sqrt{u_{11}} + r_2/\sqrt{u_{22}}},$$

$$b = \frac{u_{12} + u_{21}}{2\sqrt{u_{11}u_{22}}}, \quad c = \frac{u_{12} - u_{21}}{2\sqrt{u_{11}u_{22}}}. \tag{2.18}$$

By Eqs. (2.11) and (2.17b), one can see that the effect of the anisotropic rescaling Eq. (2.15) is to replace u_{11} and u_{22} by unity, whereas r_1 an r_2 are replaced by $1+a$ and $1-a$ respectively, while u_{12} and u_{21} are replaced by $b+c$ and $b-c$ respectively. By Eqs. (2.15) and (2.16), the polar angles of the slope vectors $\vec{M} = (M_1, M_2) = |\vec{M}|(\cos\theta, \sin\theta)$ of the original and the rescaled model are related by $\tan(\theta) = (u_{22}/u_{11})^{1/4}\tan(\theta')$, with $\tan(\theta) = M_2/M_1$ and $\tan(\theta') = M_2'/M_1'$. We note that for the case $u_{12} = u_{21}$, one has $c = 0$ by Eq. (2.18). In this case, the model Eq. (2.17) can be written in the form Eq. (2.13) employing the effective free energy, with the local potential,

$$\begin{aligned}U(M_1', M_2') = &- \frac{1+a}{2}{M_1'}^2 - \frac{1-a}{2}{M_2'}^2 \\ &+ \frac{1}{4}{M_1'}^4 + \frac{b}{2}{M_1'}^2{M_2'}^2 + \frac{1}{4}{M_2'}^4,\end{aligned} \tag{2.19}$$

generating, via Eq. (2.12a), the nonequilibrium current in Eq. (2.17b).

III. KINETIC PHASE DIAGRAM

The model in Eq. (2.17) exhibits a number of interfacial states generic for (110) crystal surfaces, as documented in its (far-from-equilibrium) phase diagram in Figs. 2 and 3. The phase diagram is deduced by linear stability analysis of the facets corresponding to the zeros of the nonequilibrium current $\vec{J}^{NE}(\vec{M})$ in Eq. (2.17b) (see Appendix A), and further corroborated by numerical simulations of the model in Eq. (2.17) (see Sec. IV). In this section, we omit primes in Eq. (2.17) for simplicity. Our model Eq. (2.17) exibits all the types of the (110) surface current zeros classified in Sec. II: (i) singlet, $M_1 = M_2 = 0$; (ii) doublets of two equivalent (symmetry related) slope vectors as in Fig. 1(d). These are the R_1 doublet, at

$$M_1 = \pm\sqrt{1+a}, \quad M_2 = 0, \tag{3.1}$$

and the R_2 doublet, at

$$M_1 = 0, \quad M_2 = \pm\sqrt{1-a}; \tag{3.2}$$

(iii) the quartet of four equivalent slope vectors, as in Fig. 1(d), at

$$M_1 = \pm\sqrt{\frac{1+c+b}{1+c^2-b^2}}\sqrt{a-a_-},$$

$$M_2 = \pm\sqrt{\frac{1-c+b}{1+c^2-b^2}}\sqrt{a_+-a}, \tag{3.3}$$

with

$$a_+ = \frac{1-b+c}{1+b-c}, \quad a_- = -\frac{1-b-c}{1+b+c}. \tag{3.4}$$

The kinetic phase diagram depends only on the three independent parameters a, b, and c in Eq. (2.18). In Figs. 2 and 3,

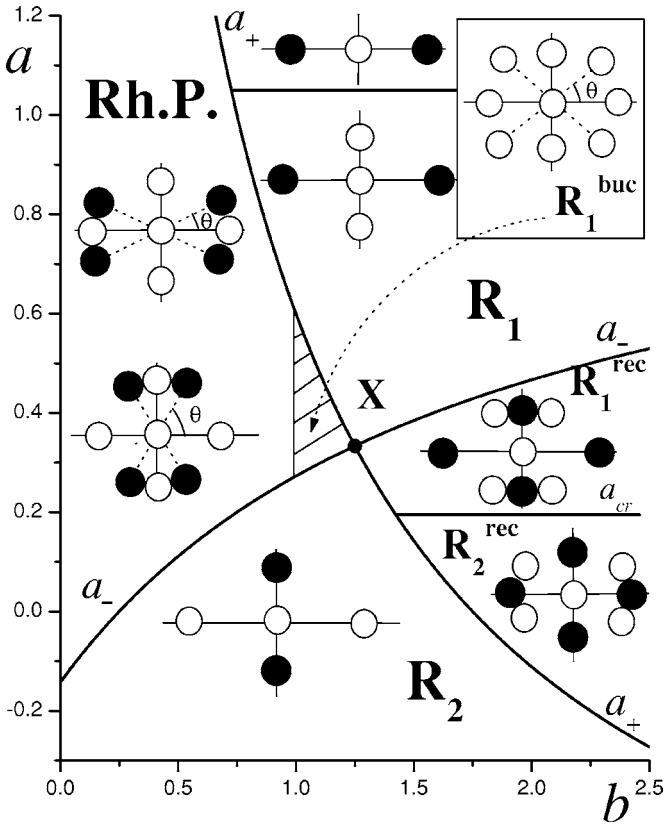

FIG. 2. Kinetic phase diagram for the multilayer epitaxial growth and erosion on (110) surfaces, as obtained from analytic arguments (Sec. III). For each interfacial state, the figure indicates M space with stable (full circles) and unstable (empty circles) zeros of the $\vec{J}^{NE}(\vec{M})$. R_1 and R_2 are the two rippled states, RhP is the rhomboidal pyramid state, $R_1^{(\mathrm{rec})}$ and $R_2^{(\mathrm{rec})}$ are the two rectangular rippled states, whereas the buckled rippled state, $R_1^{(\mathrm{buc})}$, occupies the hatched domain (*all* its current zeros are unstable, as depicted in the inset). For the RhP quartet, the angle θ ranges from zero, at the transition to R_1, to 90°, at the transition to R_2.

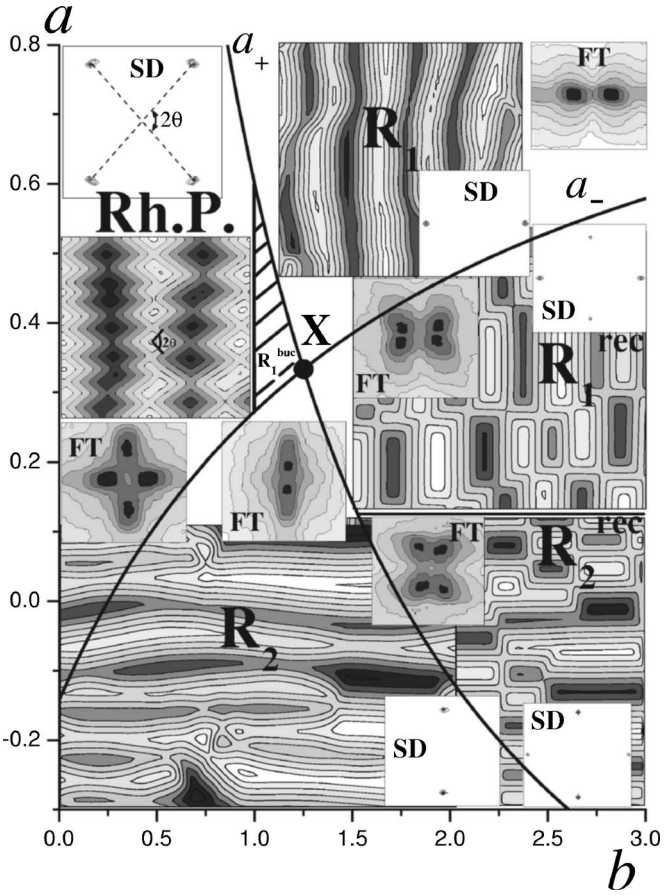

FIG. 3. Kinetic phase diagram depicting various interfacial states in terms of their basic properties (as obtained from our simulations): surface contour plots, magnitudes of interfacial height Fourier transforms (FT), corresponding to near in-phase diffraction patterns, and slope distributions (SD) in the M space, corresponding to out-of-phase diffraction patterns. R_1 and R_2 are the two rippled states, RhP is the rhomboidal pyramid state, $R_1^{(\mathrm{rec})}$ and $R_2^{(\mathrm{rec})}$ are the two rectangular rippled states, and $R_1^{(\mathrm{buc})}$ (hatched domain) is the buckled rippled state (for it, data are shown in the Figs. 8–11). The RhP rhomboidal angle 2θ ranges from zero, at the transition to R_1, to 180°, at the transition to R_2. At long times, the four-lobe FTs of the $R^{(\mathrm{rec})}$ states approach the two-lobe form of the FTs of ordinary rippled states [see Fig. 7(a)]. The peaks of SD of various states here directly correspond to the stable zeros of $\vec{J}^{NE}(\vec{M})$ in Fig. 2, with the exception of the $R_1^{(\mathrm{buc})}$ state (see Figs. 8 and 9). The phase diagram here is given for a positive value of the parameter c, without lack of generality: Changing signs of both a and c is equivalent to exchanging the base plane coordinates x_1 and x_2. Thus, in particular, the $R_1^{(\mathrm{buc})}$ state (buckled form of the R_1 rippled state) occurs for $c>0$, whereas the $R_1^{(\mathrm{buc})}$ state (buckled form of the R_2 rippled state, not shown here) occurs for $c<0$.

we depict our phase diagram in the (b,a) plane for a fixed c. In the figures, for concreteness, $c=3/4$. However, the phase diagram does not qualitatively depend on the value of c, as long as $c\neq 0$. Fig. 2 gives the stability phase diagram for the zeros of $\vec{J}^{NE}(\vec{M})$ in Eqs. (3.1)–(3.3). Figure 3, obtained from our simulations of the model Eq. (2.17), gives interface height contour plots, interface slope vector distributions (SD), and interface height Fourier transforms (FT). In the model Eq. (2.17), changing signs of both a and c is equivalent to exchanging the base plane coordinates x_1 and x_2. In effect, for a negative c, the phase diagram would appear as in the figures here reflected across the horizontal axis ($a\to -a$ reflection). Due to this, for $c=0$ the phase diagram becomes symmetric under $a\to -a$. For $a=0$ and $c=0$, the exchange of the coordinates x_1 and x_2 becomes the symmetry of the model, i.e., the model acquires the diagonal reflection symmetry that is absent on (110) surfaces. This symmetry is, however, present on (100) surfaces, and, in fact, for $a=0$ and $c=0$, the model in Eq. (2.17) reduces to that for (100) surfaces of Refs. [1,2].

The R_1 doublet Eq. (3.1) gives rise to the rippled state R_1, whereas the R_2 doublet Eq. (3.2) gives rise to the rippled state R_2, see Figs. 2 and 3. These interface states are structures of alternating facets of a doublet, e.g., for the R_1 state, the facet $(+\sqrt{1+a},0)$ alternates with the facet $(-\sqrt{1+a},0)$, see Fig. 4(a). From the stability analysis in the Appendix A, we find that the facets of the R_1 doublet are stable only for a above the line $a_+(b,c)$ in Fig. 2 [see Eq. (3.4)]. Likewise, the

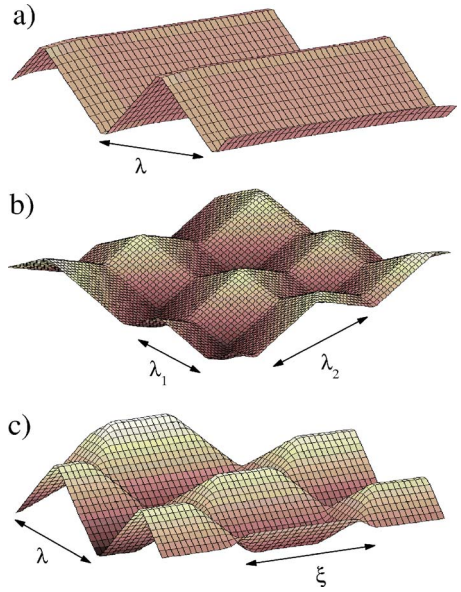

FIG. 4. (Color online) Three-dimensional (3D) views of various interfacial states from our simulations: (a) rippled state with the period λ, (b) rhomboidal pyramid state with the periods λ_1 and λ_2, and (c) rectangular rippled state, with the period λ, which motif is a rooflike pyramid (hut), with a long rooftop edge of the length ξ.

facets of the R_2 doublet are stable only below the line $a_-(b,c)$ in Fig. 2 [see Eq. (3.4)]. The lines $a_+(b,c)$ and $a_-(b,c)$ in Figs. 2 and 3 intersect at the point X located at $b_X=\sqrt{1+c^2}$, $a_X=(\sqrt{1+c^2}-1)/c$.

For $b<b_X$, in the a parameter range,

$$a_-(b,c) < a < a_+(b,c), \tag{3.5}$$

both R_1 and R_2 doublets are unstable, see Appendix A. In this range of the phase diagram in Figs. 2 and 3, both rippled phases are unstable. In Appendix A, we show that there are two types of qualitatively different stability behaviors occurring in the range in Eq. (3.5).

(i) For $b<1$, the quartet Eq. (3.3) is stable for a in the range Eq. (3.5), and, as documented in Sec. IV, it gives rise to a pyramidal state we call the rhomboidal pyramidal (RhP) state. This state is a nearly periodic structure made of four-sided pyramids, of the form

$$h(x_1,x_2) = |M_1||x_1| + |M_2||x_2|, \tag{3.6}$$

within a single period, $|x_1|<\lambda_1/2$, $|x_2|<\lambda_2/2$ [see Fig. 4(b) from our simulations]. In Eq. (3.6), (M_1,M_2) are as in Eq. (3.3). By Eq. (3.6), these pyramids have contour lines shaped as rhombs. The rhomboidal angle 2θ, between two selected quartet facets (see Figs. 2 and 3) is given by $\tan\theta=M_2/M_1$. Thus, by Eq. (3.3) we find

$$\tan\theta \sim \sqrt{\frac{a_+-a}{a-a_-}}. \tag{3.7}$$

Note, that $\theta\to 0$, i.e., $M_2\to 0$, as $a\to a_+$. In this limit, in Fig. 2 the RhP quartet Eq. (3.3) continuously approaches the R_1 doublet Eq. (3.1). Thus the R_1-to-RhP transition in Figs. 2 and 3 is a Hopf bifurcation. Also, by Eq. (3.7), $\theta\to 90°$, i.e., $M_2\to 0$, as $a\to a_-$. In this limit, in Fig. 2, the RhP quartet approaches the R_2 doublet. Thus, the R_2-to-RhP transition in Figs. 2 and 3 is also a Hopf bifurcation.

(ii) For $1<b<b_X$ and a in the range Eq. (3.5) (hatched region in Figs. 2 and 3), the Appendix A analysis indicates a rather unusual stability behavior with *all* of the types of zeros of $\vec{J}^{NE}(\vec{M})$ in Eqs. (3.1)–(3.3) unstable (see the Fig. 2 inset). This is in contrast to all other interface states entering our phase diagram, which have some of the zeros stable. The phase diagram region having all zeros unstable can never occur for the interface dynamics governed by an effective free energy F_{eff} (see Appendix A). F_{eff} exists for our model Eqs. (2,17) *only* if $u_{12}=u_{21}$, i.e. $c=0$, whereas for (110) crystal surfaces $u_{12}\neq u_{21}$ in *general*, due to the absence of the diagonal reflection symmetry (see Sec. II). Thus, importantly, the region hatched in Figs. 2 and 3, with all zeros of $\vec{J}^{NE}(\vec{M})$ being unstable, is actually generic for (110) crystal surfaces. In this region, an unusual interface state develops. It is characterized by the presence of persistent surface currents, see Sec. IV. In contrast to this so-called buckled rippled state (R^{buc}), all other states here develop facets vanishing $\vec{J}^{NE}(\vec{M})$, i.e., the facets in Eqs. (3.1)–(3.3).

There are two more interfacial states that develop in our model. In Figs. 2 and 3, they are to the right of the X point, $b>b_X$, for the parameter a in the range

$$a_+(b,c) < a < a_-(b,c). \tag{3.8}$$

In this range, the R_1 and R_2 facets in Eqs. (3.1) and (3.2) are *both* stable, while the quartet Eq. (3.3) is unstable. From our simulations in Sec. IV, we find that, in the *multistable* region Eq. (3.8), interface structures formed out of both R_1 and R_2 facets develop. These structures have rectangular countour lines (see Fig. 3) corresponding to rooflike pyramids (huts) with long rooftop edges, see Fig. 4(c). As seen in Fig. 3, there are two kinds of these structures, called as the rectangular rippled states $R_1^{(\mathrm{rec})}$ and $R_2^{(\mathrm{rec})}$: in the $R_1^{(\mathrm{rec})}$ state, the R_1 facets grow faster than R_2 facets, whereas in the $R_2^{(\mathrm{rec})}$ state, the R_2 facets grow faster than R_1 facets. The difference in the growth rates between the facets is related to the fact that R_1 facets, Eq. (3.1), and R_2 facets, Eq. (3.2), are not equivalent to each other. The diagonal reflection that would make them equivalent is not a symmetry of (110) surface, see Eq. (2.10). This suggests that, *in general*, there is no a steady state interface profile ($\partial h/\partial t=0$) of the dynamics equation (2.1) that would have the form of a *static* edge between the nonequivalent R_1 and R_2 facets (so one of them prevails, as seen in the $R^{(\mathrm{rec})}$ states). Indeed, such a static edge can exist only along the special line $a_{cr}(b,c)$ in the phase diagram Fig. 2, given by the equation,

$$a_{cr} = \frac{\sqrt{1+(c/3)^2}-1}{c/3}, \tag{3.9}$$

derived in Appendix B. The critical line Eq. (3.9) actually corresponds to the phase transition between $R_1^{(\mathrm{rec})}$ and $R_2^{(\mathrm{rec})}$ states in Figs. 2 and 3; see Sec. IV. In Appendix B, we also prove a theorem on the existence of static edges between two facets with preferred slope vectors $\vec{M}_A$ and $\vec{M}_B$ [i.e.,

$\vec{J}^{NE}(\vec{M}_A)=\vec{0}$ and $\vec{J}^{NE}(\vec{M}_B)=\vec{0}$], for the model Eq. (2.1) with a general form of the $\vec{J}^{NE}(\vec{M})$ and the curvature current of the surface diffusion type (see Sec. II). For this class of models, our theorem asserts that the static edge exists provided

$$\int_{\vec{M}_A}^{\vec{M}_B} d\vec{M}\cdot\vec{J}^{NE}(\vec{M})=0. \tag{3.10}$$

In the line integral in Eq. (3.10), the integration path (in the M space) is the *straight* line segment connecting tips of the vectors $\vec{M}_A$ and $\vec{M}_B$ (see Appendix B and Fig. 12 therein). For the special case with the nonequilibrium current generated by a potential $U(\vec{M})$, via Eq. (2.12a), our theorem Eq. (3.10) reduces to the condition $U(\vec{M}_A)=U(\vec{M}_B)$ analogous to the standard Gibbs condition of (effective) free energy density equality at the first-order transitions between two different phases. However, the F_{eff} exists here only under special circumstances, that is, if the parameter c in the model Eq. (2.17) vanishes, see Sec. II. Thus, to discuss the general situation with $c\neq 0$, we must invoke the more general theorem on the static edges existence in Eq. (3.10). We stress that if the facet slopes $\vec{M}_A$ and $\vec{M}_B$ are two equivalent vectors (related by a surface symmetry operation) then, by invoking the current symmetries Eqs. (2.6)–(2.9), the Eq. (3.10) can be shown to be automatically satisfied [in contrast to nonequivalent facets which coexistence requires special conditions such as Eq. (3.9)]. Significant examples for this unrestricted facet coexistence are the static edges formed between the two facets of the R_1 (or R_2) doublet seen in the R_1 (respectively R_2) rippled phase, and the static edges between any two of the four quartet facets (seen in the RhP state). In fact, thanks to this coexistence, the four-sided RhP pyramids are structurally *possible*.

We end this section with a few conceptually and physically significant notes.

(1) An important aspect of the epitaxial growth is the selection of the slope vectors of the faceted morphologies developing across the interface. In numerous previos studies, the selected facet slope vectors are simply assumed to correspond to the zeros of $\vec{J}^{NE}(\vec{M})$. We stress, however, that this common "zero current assumption" is necessarily true only for the interface dynamics governed by an effective free energy: By Eqs. (2.12) and (2.13), it can be shown that $dF_{eff}/dt=-\int d^2x(\partial h/\partial t)^2\leqslant 0$, i.e., F_{eff} generally decreases in time. This time minimization of F_{eff} is achieved by breaking up of the interface into (growing) flat facets: on a flat facet the surface diffusion "free energy" $F_{SD}\geqslant 0$, Eq. (2.13c) reduces to zero, whereas the nonequilibrium current "free energy" Eq. (2.13b) is minimized by selecting the slopes that minimize the local potential $U(\vec{M})$. Thus, by Eq. (2.12a), $\vec{J}^{NE}=0$ at the selected slope vectors. On the other hand, in our model, unless $c=0$, there is *no* F_{eff} governing the interface dynamics. Thus, for $c\neq 0$, it is *not* assured that interface structures have facets vanishing $\vec{J}^{NE}(\vec{M})$. This is evidenced here by the existence of our $R^{(buc)}$ state, which indeed exhibits persistent surface currents (see Sec. IV). Still, with this important exception, for all other states of our model we find that the selected facet slopes $\vec{M}$ are zeros of $\vec{J}^{NE}(\vec{M})$.

(2) For the special yet conceptually significant case $c=0$, i.e., $u_{12}=u_{21}$, whence interface dynamics is governed by an F_{eff} [see Eqs. (2.12), (2.13), and (2.19)], the phase diagram in the (b,a) plane becomes symmetric with respect to $(b,a)\rightarrow(b,-a)$, with the axis $a=0$ becoming the symmetry axis of the phase diagram. For $c=0$, the change $a\rightarrow -a$ is equivalent to exchanging x_1 and x_2, as can be seen from Eq. (2.17). In particular, R_1 state is then mapped into R_2 state. Likewise, $R_1^{(rec)}$ is mapped into $R_2^{(rec)}$ and the transition line between these states is simply $a_{cr}=0$, in accord with Eq. (3.9) for $c\rightarrow 0$. Indeed, for $c=0$, selected slopes are minima of the potential $U(M_1,M_2)$ in Eq. (2.19). At $a=0$ and for any $b>1$, $U(M_1,M_2)$ has two degenerate minima at the slope vectors $\vec{M}_A=(\pm 1,0)$ and $\vec{M}_B=(0,\pm 1)$ [see Eqs. (3.1) and (3.2) with $a=0$], i.e., $U(\vec{M}_A)=U(\vec{M}_B)$, so the system is *at* the phase transition between $R_1^{(rec)}$ and $R_2^{(rec)}$ states. At this transition, $\vec{M}_A$ and $\vec{M}_B$ facets coexist and this gives rise to the formation of a four-sided pyramidal state occurring at this critical point (see also Sec. IV). On the other hand, a positive a in Eq. (2.19) would break the degeneracy in favor of the $\vec{M}_A$ facet that then has a smaller effective free energy density Eq. (2.19) than the $\vec{M}_B$ facet. This gives rise to the formation of the $R_1^{(rec)}$ phase, with the dominant $\vec{M}_A$, i.e., R_1 facets outgrowing smaller, less rapidly growing $\vec{M}_B$, i.e., R_2 facets; see Sec. IV. Likewise, for $a<0$, the $R_2^{(rec)}$ phase is favored, with the dominant R_2 facets outgrowing smaller, less rapidly growing R_1 facets. All these trends can be easily understood in terms of the F_{eff}, i.e., the potential Eq. (2.19) that exists for $c=0$, and ensures that the phase transition is governed by the free energy minimization. It is, however, remarkable that a similar first-order transition phenomenon occurs for $c\neq 0$ as well, in the absence of an exact F_{eff}. A nonzero c causes just a shift of the critical value a_{cr} from zero to the nonzero value given by Eq. (3.9).

(3) The buckled rippled state occuring in the range $1<b<b_X=\sqrt{1+c^2}$ (the hatched area in Fig. 2) disappears for vanishing c. It is the existence of F_{eff} that excludes (for $c=0$) the situation with all zeros of $\vec{J}^{NE}(\vec{M})$ being unstable, which occurrs in the buckled rippled state (see Appendix A). We stress, however, that, due to *ubiquitous* diagonal asymmetry Eq. (2.12), one has $c\neq 0$ (i.e., nonexistence of F_{eff}) in general on (110) surfaces. This fact *ensures the presence* of the Buckled Rippled State in the overall phenomenological phase diagram for (110) surfaces epitaxial growth and erosion.

IV. INTERFACIAL STATES

In this section, we discuss the properties of the multitude of interfacial states introduced in Sec. III. We begin with the rhomboidal pyramid (*RhP*) state which is a *two-dimensional* periodic interface structure of four-sided pyramidlike objects seen in Fig. 4(b) with the form given by Eq. (3.6). The contour lines (i.e., step terraces) of these pyramids are *rhombi* that occasionally transform into *rhomboids*, if rooftop edges develop on the pyramids, see Fig. 5. This *RhP* state, pre-

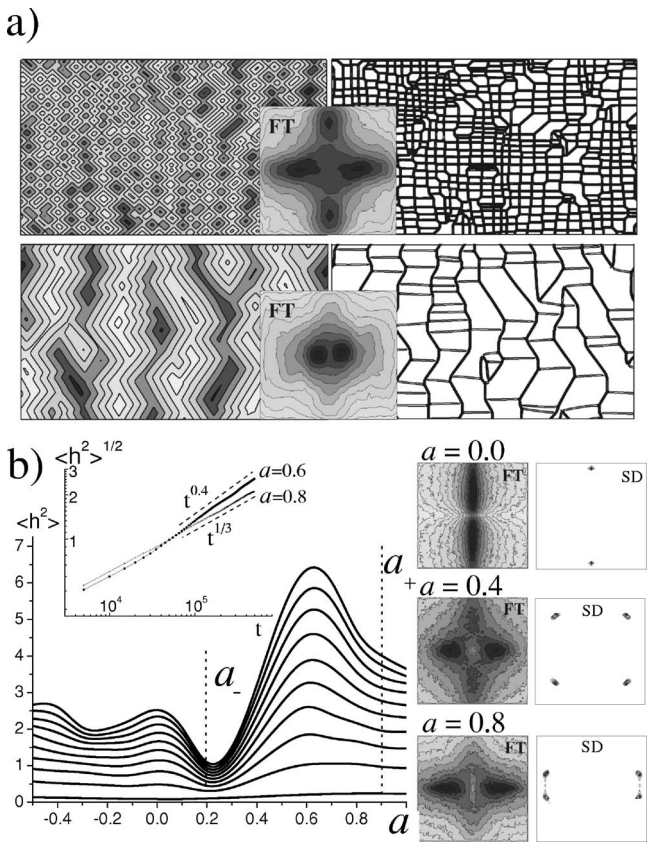

FIG. 5. (a) Rhomboidal pyramid (*RhP*) state: To the left, the interface contour plots. To the right, facet edges plots (contour plots of the magnitude of local interface curvature), with prominently present dislocations destroying perfect periodicity of the interface profile. In the upper panel of (a), we give the ordinary RhP state, occurring away from the *RhP*-to-$R_1^{(\mathrm{buc})}$ transition. In the lower panel of (a), we give the intensely rough RhP state, occurring close to this transition [the interface here corresponds to the maximally rough surface found at $a=0.6$ in (b) here]. Note the qualitative difference between the FTs in the upper and lower panels of (a), see the text. (b) The square of the interfacial width $\langle h^2\rangle$ vs the parameter a, given for several different times, across the transition from the rippled state R_2 (for $a<a_-$) to the rippled state R_1 (for $a>a_+$), going through the intermediary rhomboidal pyramid state (occurring for $a_-<a<a_+$). The figure is obtained from numerous simulations done along the line $b=0.8$ that passes close to the transition line $b=1$ from the *RhP* to the $R_1^{(\mathrm{buc})}$ state (see Figs. 2 and 3). The inset documents the enhanced roughening of the *RhP* state, with the roughening exponent reaching the value ≈ 0.4 close to the center of the RhP range, at $a=0.6$. In (b), to the right, we give FT magnitudes and SDs found along this ripple rotation transition, for $a=0$ (in the R_2 state), and for $a=0.4$ and 0.8 (both within the intensely rough *RhP* range). Note that FTs, i.e., in-phase diffraction patterns of the intensely rough *RhP* are with just one pair of peaks, like the R_1 pattern. The other, significantly weaker pair of peaks can be seen only close to the transition to R_2 (see $a=0.4$ here). Note that SDs, i.e., the out-of-phase diffraction patterns distinguish the *RhP* from the R_1 state (see Fig. 3).

dicted by us in Ref. [3], has been subsequently seen by de Mongeot and co-workers in the epitaxial erosion on both Cu(110) and Rh(110) surfaces [13]. Typical for the *RhP* state is the interface slope distribution (SD) (i.e., out-of-phase diffraction pattern) with the quartet of four equivalent peaks $(\pm M_1, \pm M_2)$, see Figs. 3 and 5. By the *RhP* motif in Eq. (3.6), squared magnitude of the Fourier transform (FT), $|\tilde{h}(q_1,q_2)|^2$ of the *RhP* 2D periodic surface is easily shown to have dominant peaks placed along the q_1 and q_2 axes: (i) the set of peaks at the wave vectors $[\pm 2\pi(2n+1)/\lambda_1, 0]$, with the integrated intensities $I_n^{(1)} \sim (M_1\lambda_1)^2(2n+1)^{-4}$, $n=0,1,2,\ldots$; (ii) the set of peaks at $[0, \pm 2\pi(2n+1)/\lambda_2]$ with the integrated intensities $I_n^{(2)} \sim (M_2\lambda_2)^2(2n+1)^{-4}$, $n=0,1,2,\ldots$. Structurally, by Eq. (3.6), the *RhP* state has the form of a linear superposition of the two rippled states. Thus, its FT (i.e., experimentally, the near in-phase diffraction pattern) is essentially the superposition of the FTs of the two rippled states R_1 and R_2 (see Fig. 3). Notably from our simulations, (at most) the four brightest ($n=0$) among the peaks, at the wave vectors $(\pm 2\pi/\lambda_1, 0)$ and $(0, \pm 2\pi/\lambda_2)$ are visible (see Fig. 5). Such a four-lobe near in-phase diffraction pattern is manifested in the *RhP* FT magnitude plots in Fig. 3 and in the upper panel of Fig. 5(a) from our simulations. All other peaks are smeared by the positional disorder of the pyramid lattice. This disorder is especially pronounced in the *RhP* region close to the $R_1^{(\mathrm{buc})}$ state. Therein, the *RhP* in-phase diffraction pattern exhibits only two peaks [unless very close to the *RhP*-to-R_2 transition, see the lower panel in Fig. 5(a) and see Fig. 5(b), and the discussions in the following]. Such a nearly two-lobe *RhP* near in-phase diffraction pattern has been indeed seen in the recent study that has revealed our *RhP* state in erosion on Cu(110) and Rh(110) crystal surfaces [13].

The *RhP* state is characterized by (nearly) rectangular network of pyramid facet edges, see Fig. 5(a). The coarsening dynamics of the *RhP* state is similar to that of the square pyramid Phase I (with the square network of edges) on (001) surfaces [1,4]. The coarsening is mediated by motion and annihilations of the dislocations of the network of pyramid facet edges seen in Fig. 5(a). In accord with this, we find that the interface width, $w=\langle h^2\rangle^{1/2}$, grows as $w \sim t^{\beta}$, with $\beta \approx 1/4$ [1,4]. Such a coarsening was found *away* from the transitions to other interface states in Figs. 2 and 3, whence the *RhP* forms as in the upper panel of Fig. 5(a). However, a substantially faster coarsening was found in the *RhP* region close to the $R^{(\mathrm{buc})}$ state (the hatched domain in Figs. 2 and 3, discussed later on). This enhanced roughening of *RhP* is documented in Fig. 5(b), which gives the interface width w for several different times, versus the parameter a (for a fixed $b<1$). In this figure, the *RhP* state occurs between a_+ and a_-, whereas for $a<a_-$ $(a>a_+)$ one has the rippled phase R_2 (respectively, R_1) occurs. The fastest coarsening was found within the RhP state range, $a_-<a<a_+$; see Fig 5(b). Therein, at the longest times, the *RhP* pyramids grow with a high coarsening exponent $\beta \approx 0.4$, see Fig 5(b). Such an enhanced roughening of the *RhP* intermediary state (faster than that of the nearby rippled states, see below) has been observed also in the aforementioned experiments on Cu(110) and Rh(110) surfaces [13]. We stress that the enhanced roughening of *RhP* occurs only in the proximity to the $R^{(buc)}$ state in Figs. 2 and 3. There, the *RhP* state becomes highly anisotropic. This is documented in the lower panel of Fig. 5(a) where we see that the two *RhP* state periods λ_1 and λ_2

[along the principal axis of (110) surface, see Fig. 4], significantly differ from each other. This anisotropy is manifested also in the character of the pyramid edges seen in the lower panel of Fig. 5(a): vertical edges are sharp and connected to each other (either directly or by frequently present rooftop edges). In contrast to this, the horizontal edges seen in this figure are blunt and disconnected from each other. Due to this positional disorder of horizontal edges, the intensely rough *RhP* structure in the lower panel of Fig. 5(a) is significantly more disordered then the ordinary *RhP* structures seen in the upper panel of Fig. 5(a). Its enhanced roughening is similar to the fast roughening seen in the nearby $R^{(\mathrm{buc})}$ state, discussed later in this section. Both the intensely rough *RhP* and the $R^{(\mathrm{buc})}$ state exhibit two-lobe near in-phase diffraction patterns (i.e., FT's), see Fig. 5, as well as Fig. 11 later on. Having the two-lobe (rather than the four-lobe) FT pattern is a consequence of the typically large aspect ratio λ_1/λ_2, and also, of the strong positional disorder of vertical facet edges manifest in the lower panel of Fig. 5(a). Indeed, by our previous discussions of the peak intensities, $I_0^{(2)}/I_0^{(1)} = (M_2\lambda_2)^2/(M_1\lambda_1)^2$, so for $\lambda_2 \ll \lambda_1$ the peak pair at $(q_1=0, q_2=\pm 2\pi/\lambda_2)$ is much weaker than the peak pair at $(q_1 = \pm 2\pi/\lambda_1, q_2=0)$. The weaker peak pair is thus easily depressed by the positional disorder seen in the lower panel of Fig. 5(a). In effect, the intensely rough *RhP* state exhibits the two-lobe near in-phase diffraction patterns seen in Fig. 5. Thus, importantly, the intensely rough *RhP* state has nearly the same in-phase diffraction pattern as a simple rippled state. This feature, seen in the experiments on Cu(110) and Rh(110) surfaces [13], is documented here in Fig. 5(b) from our simulations. Note that this FT, i.e., the near in-phase diffraction pattern, is nearly the same as that of the R_1 rippled state [unless close to the transition to the R_2 rippled state, see the middle panel of Fig. 5(b)]. Because of this, the out-of-phase diffraction pattern, i.e., slope distribution from our simulations [see Fig. 5(b)], with the quartet of four equivalent peaks, is essential for the identification of our *RhP* state. This is confirmed by the recent experiments on Cu(110) and Rh(110) surfaces [13]. Our R_1 state here corresponds to the "hot rippled state" (the high temperature one), whereas the experiments indeed show that the *RhP* has the same FT as the "cold ripple state" seen in Ref. [13].

We now proceed to discuss the properties of the rippled states R_1 and R_2. From our simulations we find that the coarsening of the rippled states is mediated by moving dislocations that destroy the perfect periodicity of these structures. See Figs. 6(a) and 6(b), giving the interface in terms of the edges formed between alternating *R* facets [see also Fig. 4(a)]. The dislocations of rippled states R_1 and R_2 are somewhat similar to the dislocations of 2D smectic A liquid crystals [15]. Here, however, the dislocations are prominently dynamical objects. They move (climb) along the direction of facet edges in Figs. 6(a) and 6(b). This motion is driven by the edges tensions, which are unbalanced at the dislocations cores. In Figs. 6(a) and 6(b) we see two morphologically different types of dislocations: (i) "forks," with three edges on one side of the core and just one edge on the opposite side; (ii) "knives," with two edges on one side and no edges on the opposite side of the core. Thus, in both cases, there are extra two edges pulling dislocations. This misbalance of

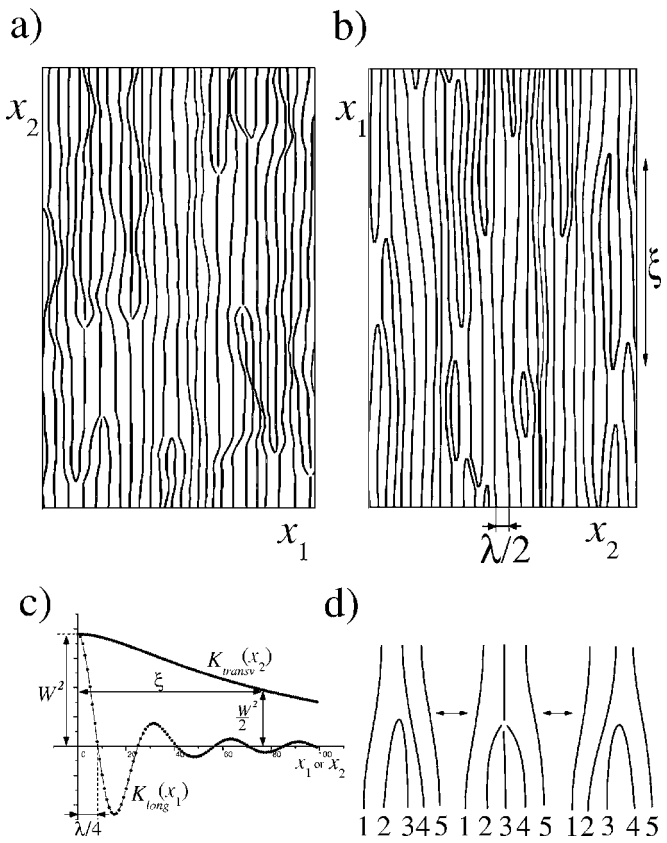

FIG. 6. (a) Facet edges plot of the rippled state R_1 in the phase diagram domain in which both fork and knife dislocations are present. (b) Facet edges plot of the rippled state R_2 in the domain in which only knife dislocations occur. Note that the R_2 state in (b) is rotated by 90° to facilitate comparison with (a). The length scale ξ is the average distance between dislocations along a ripple, see the text. (c) Rippled states interface height-height correlation functions $K(x_1,x_2,t)$ of the R_1 state: Longitudinal correlations $K_{long}(x_1,t) = K(x_1,x_2=0,t)$, used to find the average phase period $\lambda(t)$, and transversal correlations $K_{trans}(x_2,t)=K(x_1=0,x_2,t)$ used to find the ripple coherence length $\xi(t)$. (For the R_2 state, x_1 and x_2 are to be switched in the above statements.) In (d) we depict topological changes (knife-to-fork-to-knife transitions) causing the dislocation to glide by one half of the ripple phase period. Such a dislocation glide is prohibited if fork formation is suppressed, as in the rippled state in (b).

edges tensions causes the dislocations to move along the ripples, i.e., vertically in Figs. 6(a) and 6(b). Importantly, we find that this dislocation motion (climb) mediates the growth of the ripple phase period λ: as the dislocation climbs along the extra edges, it leaves behind enlarged facets [compare the facet width just above and below dislocations in Figs. 6(a) and 6(b)]. Thus, the growth of the rippled phase period λ is nothing else but the fusion of the rippled state *R* facets mediated by climbing dislocations in Figs. 6(a) and 6(b).

In addition to the interface width *w* and the average ripple period λ, we find that the rippled states are characterized also by the *coherence length* of ripples, ξ, corresponding to the separation between dislocations along a ripple (see Fig. 6). The ripple coherence length ξ increases with time because of annihilations of pairs of dislocations traveling towards each

other in Figs. 6(a) and 6(b). Due to the annihilations, the number of dislocations decreases, and the ripple coherence length ξ increases in time. Both λ and ξ are extracted from our simulations by computing the anisotropic height-height correlation function,

$$K(x_1,x_2,t) = \langle h(x_1,x_2,t)h(0,0,t)\rangle = [w(t)]^2\psi[x_1/\lambda(t),x_2/\xi(t)], \tag{4.1}$$

for the R_1 phase. In Eq. (4.1), the function ψ decays in an oscillatory fashion along x_1 (longitudinal correlations), and monotonously along x_2 (transversal correlations) see Fig. 6(c) for details. By using the longitudinal and transversal correlations, from our simulations we find that $\lambda \sim w$ and ξ grow as power laws of time,

$$w \sim \lambda \sim t^{n_\lambda}, \quad \xi \sim t^{n_\xi}. \tag{4.2}$$

Regarding the values of the coarsening exponents $\beta=n_\lambda$ and n_ξ, we have revealed *two* kinetically different subdomains of the whole rippled phase domain in the phase diagram in Fig. 4. The two subdomains are characterized by different morphologies and kinetics of moving dislocations, as illustrated in Figs. 6(a) and 6(b). Most of our phase diagram in Fig. 3 is occupied by the rippled phase with the dislocations depicted in Fig. 6(a). In this figure, we see both forks and knives climbing along the x_2 direction. In addition to this directed climbing motion, our simulations reveal that dislocations move also along the x_1 direction in Fig. 6(a). In contrast to the steady dislocation climb, the dislocation glide motion along x_1 has a random walk character and it involves reconnection (topology changes) of the edges network, turning forks into knives and vice versa; see Fig. 6(d). There we see a knife turning into a fork, which then turns into a knife, the position of which is displaced by one half of the rippled phase period (with respect to the position of the original knife). In the subdomain of the phase diagram in which such a mechanism of dislocation glide is active, we find that the $w \sim \lambda$ and ξ grow as in Eq. (4.2) with $\beta=n_\lambda=2/7$ and $n_\xi=4/7$, from our simulations, and further corroborated by analytic arguments elsewhere [16]. Our simulations, however, reveal the existence of another subdomain of the kinetic phase diagram in Fig. 3, in which the coarsening of the rippled phase goes with different exponents, $n_\lambda=1/3$ and $n_\xi=1/2$. This scaling was found to occur for $c \neq 0$ in a range below the *RhP* domain in Fig. 3 [e.g., for a below a_-, i.e., below the intensely rough *RhP* in Fig. 5(b)]. Therein, the reconnections of facet edges (i.e., the formations of forks) are suppressed, as documented in Fig. 6(b) from our simulations in which only the knife-dislocations are seen. Consequently, the dislocation glide motion [Fig. 6(d)] is prohibited in this subdomain of the phase diagram. This dynamical constraint yields the aforementioned exponents $\beta=n_\lambda=1/3$ and $n_\xi=1/2$ found in the simulations and further corroborated by analytic arguments elsewhere [16]. In contrast to the long time (slope selection dominated) regime with $\beta=n_\lambda$, in the ion erosion studies on Cu (110)[13], the selected facets of the rippled and the *RhP* state have not yet fully reached the selected slope magnitudes (their slope angle still grows within the experimental time window). We stress that such

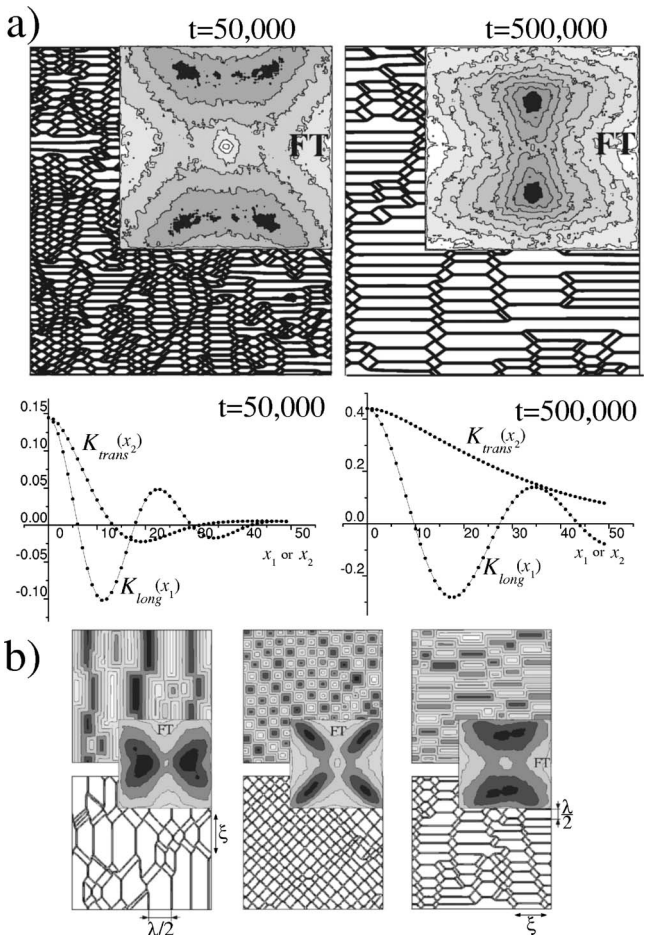

FIG. 7. Rectangular rippled states: (a) Snapshots of facet edges plots of the $R_2^{(rec)}$ state and interface FTs at two different times, and corresponding longitudinal and transversal correlations used to obtain the structural length scales $\lambda(t)$ and $\xi(t)$ [using the recipe in Fig. 6(c)]. Note the presence of rapidly growing horizontal rooftop edges interfacing the dominant R_2 facets [see also Fig. 5(c)]. These rooflike pyramids (huts) are terminated on both sides by small rhomboidally shaped R_1 facets which cluster to form long chains. (b) Sequence of interfacial states occurring in the $R_1^{(rec)}$ to $R_2^{(rec)}$ transition (interface contour lines and corresponding facet edges plots). For $a > a_{cr}$, one has the $R_1^{(rec)}$ state with rooftop edges growing vertically (left panel). For $a < a_{cr}$, one has the $R_2^{(rec)}$ state with rooftop edges growing horizontally (right panel). At the critical point $a=a_{cr}$, four-sided rectangular pyramids develop with no rooftop edges present (middle panel).

early time regimes are known to exhibit the coarsening exponent n smaller than β, with a typically small n [17].

In addition to passing through the *RhP* and the $R^{(buc)}$ states, the transition between the rippled states R_1 to R_2 may go also through the rectangular rippled states, $R_1^{(rec)}$ and $R_2^{(rec)}$ comprised of rooflike pyramids (huts) formed out of both R_1 and R_2 facets, see Figs. 3, 4(c), and 7. We stress that our basic $R^{(rec)}$ state structure, the checkerboard arrangement of huts and pits (inverted huts) has been clearly seen in the erosion experiments on Ag(110), by Constantini *et al.* [see Fig. 4(d) in Ref. [10], and compare with our Figs. 3 and 7]. The hut sizes λ and ξ are measured along the two (non-

equivalent) principal directions of (110) surface [see Figs. 4(c) and 7]. We find they grow in time with *different* power laws: $\lambda \sim t^{n_\lambda}$, with $n_\lambda = 1/4$, and $\xi \sim t^{n_\xi}$, with $n_\xi = 1/2$, as obtained from the longitudinal and transversal height correlations [Fig. 7(a)]. As $w(t) \sim \lambda(t) \ll \xi(t)$ at long times, such $R^{(\mathrm{rec})}$ pyramid states are a special kind of rippled states with the period $\lambda(t)$. This is evidenced by their Fourier transforms, i.e., near in-phase diffraction patterns seen in Fig. 7(a). They have four peaks, at $(\pm q_1, \pm q_2)$, with $q_1 \sim 1/\lambda$ and $q_2 \sim 1/\xi$, for the $R_1^{(\mathrm{rec})}$ state. However, as $\xi(t) \gg \lambda(t)$, this diffraction pattern approaches in time the form of the near in-phase diffraction pattern of the nearby rippled R_1 state with just two peaks at $(\pm q_1, 0)$. The length scale $\xi(t)$ is essentially the length of the long rooftop edges present on these rooflike pyramids, see Figs. 7 and 4(c). These rooftop edges develop and grow either along the x_2 direction in the $R_1^{(\mathrm{rec})}$, or along the x_1 direction in the $R_2^{(\mathrm{rec})}$ state, see Fig. 7(b). The snapshots form our simulations of the $R_2^{(\mathrm{rec})}$ state, in Fig. 7(a), well document the presence of rapidly growing horizontal rooftop edges interfacing the dominant R_2 facets. Note that these rooflike pyramids (huts) are terminated on both sides by small rhomboidally (diamond) shaped R_1 facets. Prominent feature of the $R^{(\mathrm{rec})}$ state is that these diamondlike facets cluster to form long chains. Due to the presence of these facet chains, the interface structure of the $R^{(\mathrm{rec})}$ states is more coherent than that of ordinary rippled states. At early times, $R^{(\mathrm{rec})}$ states appear periodiclike not only along the λ direction but also along the ξ direction (unlike the ordinary rippled phase): Note that, at early times, the transversal correlations in Fig. 7(a) oscillate [unlike the correlations of the ordinary rippled state in Fig. 6(c)]. However, with increasing time, the number of diamond facets clustered into each of the chains decreases and, also, the diamond facets chains are less evenly spaced, as seen in Fig. 7(a). Due to this, the coherence of the $R^{(\mathrm{rec})}$ state along the transversal direction (parallel to ripples) decreases in time and becomes comparable to that of ordinary rippled state. This is manifested in the loss of oscillations in the transversal height correlations [see Fig. 7(a) at the long time and compare with Fig. 6(c)]. Related to this, at long times, the four FT peaks of the $R^{(\mathrm{rec})}$ state in the left panel of Fig. 7(a) merge into just two peaks seen in the right panel, and such FT becomes indistinguishable from that of the ordinary rippled state (see Fig. 4).

The rooftop edges on the rectangular pyramids do not develop only at the transition between $R_1^{(\mathrm{rec})}$ and $R_2^{(\mathrm{rec})}$ states in Figs. 2 and 3; see Fig. 7(b). At this transition, simple four-sided pyramids (without rooftop edges) develop, with a rhomboidal network of edges, see the middle panel of Fig. 7(b). This critical state is an anisotropic version of the square pyramid Phase II on (100) surfaces [1,4]. Its near in-phase diffraction pattern has four peaks $(\pm q_1, \pm q_2)$, with $q_1 \sim q_2 \sim 1/t^{1/4}$. The $R_1^{(\mathrm{rec})}$-to-$R_2^{(\mathrm{rec})}$ transition line is a far-from-equilibrium first-order-like transition at which the two nonequivalent doublets of (110) surfaces [see Eqs. (3.1) and (3.2), and Fig. 1(d)] coexist. This coexistence is necessary to ensure the structural stability of the four-sided pyramids developing at the transition point. Indeed, R_1 and R_2 facets comprising such pyramids can maintain (at long times) equal sizes and shapes only if the conditions are fulfilled to have the stationary solution $(\partial h/\partial t = 0)$ of Eq. (2.1) being the static interface (edge) between two *semi-infinite* R_1 and R_2 facets. As noted in Sec. III, this requirement yields our analytic prediction for the position of the $R_1^{(\mathrm{rec})}$-to-$R_2^{(\mathrm{rec})}$ transition line given in Eq. (3.9), which is corroborated by the simulations in Fig. 7(b). Main features of the ripple rotation transition seen on Ag(110) surface (growth) [9] correspond to those of our $R_1^{(\mathrm{rec})}$-to-$R_2^{(\mathrm{rec})}$ transition. Importantly, our study shows that in the multistable region (suggested by the experiments Ref. [9]) one deals *not* with simple rippled phases (R_1 and R_2) but rather with more complex structures, the rectangular rippled states. We note that the intermediary state seen on Ag(110) has a near in-phase diffraction pattern different from that of the critical state seen in the middle of Fig. 7(b). Still, the experimental out-of-phase pattern is the same as for the state in the middle of Fig. 7(b). As we discussed elsewhere [18], the experimental near in-phase diffraction pattern (as observed in Ref. [9] close to the transition) emerges due to an interesting effect of the vertical growth asymmetry between the huts and pits (inverted huts) comprising the $R^{(\mathrm{rec})}$ state interfaces.

Our model exhibits one more state, the buckled rippled $R^{(\mathrm{buc})}$ state, which occupies the hatched region in Figs. 2 and 3. Therein, as discussed in Sec. III and Appendix A, *all* zeros of $\vec{J}^{(NE)}(\vec{M})$ are *unstable* (in contrast to the rest of the phase diagram, with at least some zeros stable). The very existence of such a state escapes the common belief that the stable facets with vanishing $\vec{J}^{(NE)}(\vec{M})$ dominate the epitaxial growth and erosion with slope selection (as no facet is stable here). In the region of our $R^{(\mathrm{buc})}$ state in Figs. 2 and 3, we find a long transient involving ordering of pyramidal chains, see Fig. 8. The interface eventually selects the shape of a rippled phase with buckled (wavy) ripples. The buckling breaks the ripples into smaller facets joined by edges, see Fig. 9(a). Due to this, the $R^{(\mathrm{buc})}$ state is structurally close to the *RhP* state, with a motif similar to that of *RhP*, Eq. (3.6), however with M_1 and M_2 therein *not* corresponding to a zero of $\vec{J}^{(NE)}(\vec{M})$, see Fig. 8(c). Thus, strikingly, in contrast to the RhP and all other states discussed here, the $R^{(\mathrm{buc})}$ state does not develop facets whose slopes vanish $\vec{J}^{(NE)}(\vec{M})$, see Figs. 8(c) and 9. Rather, as documented in Fig. 9, the facets of the $R^{(\mathrm{buc})}$ state carry nonvanishing, *persistent* downhill surface currents. The downhill currents in the $R^{(\mathrm{buc})}$ facets are compensated by uphill currents flowing along the edges between the facets, i.e., the net current flux is *zero*; see Fig. 9(c). Due to these current backflows, the overall surface current pattern has a *vortexlike* character, with vortices forming a rectangular lattice; see Fig. 9(b). As seen in this figure, the $R^{(\mathrm{buc})}$ state exhibits both clockwise and counterclockwise oriented vortices alternating across the surface. This *convectionlike* surface current pattern, driven by incoming atomic fluxes, is a far-from-equilibrium relative of the self-organized fluid patterns formed in the hydrodynamic systems exhibiting convective instabilities driven by heat fluxes, e.g., Rayleigh-Benard patterns [19]. Note, however, that, unlike these steady hydrodynamic patterns, the length scales of the $R^{(\mathrm{buc})}$ state vortex lattice actually grow in time as the interface coarsens. In the $R^{(\mathrm{buc})}$ state, the distribution of interface slope vectors

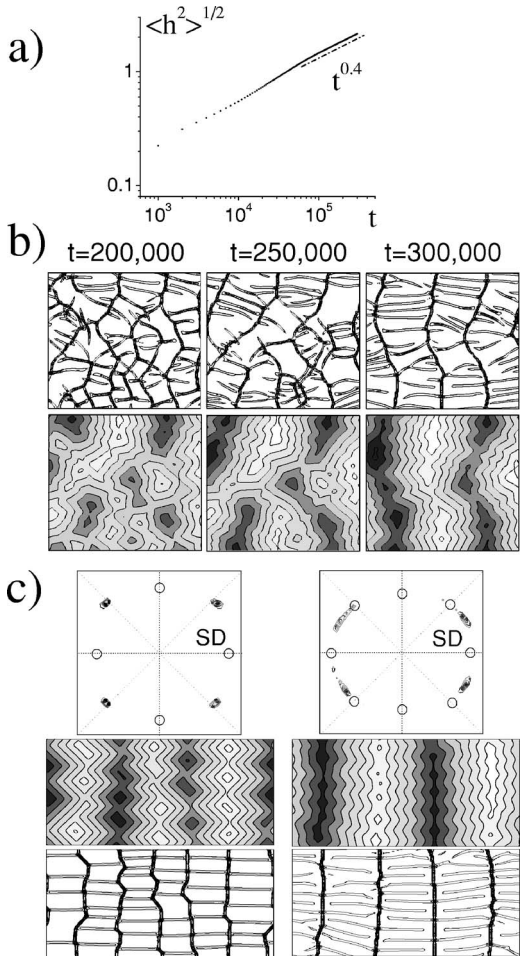

FIG. 8. Buckled rippled state. (a) Its interfacial width $w=\langle h^2\rangle^{1/2}$ grows rapidly in time, $w\sim t^{\beta}$ with a high coarsening exponent $\beta\approx 0.4$. (b) Time evolution of the interface, through its contour plots (upper panels) and facet edges plots (lower panels). Note that a regular interface structure develops at long time scales (see the text and Fig. 9). (c) Rhomboidal pyramid state (left panels) and the buckled rippled state (right panels) have similar interface morphologies as evidenced by their SDs in M space (top), their interfacial contour plots (middle), and corresponding facet edges plots (bottom). For both states, we put the quartet zeros of the surface nonequilibrium current on the dashed lines guiding the eye. Note, from (c) right panel, that the buckled rippled state SD has peaks that are *off* the zeros of the current (indicated by open circles). Thus, in contrast to the rhomboidal pyramid state in the left panel in (c), the facets of the buckled rippled state carry persistent surface currents (see also Fig. 9).

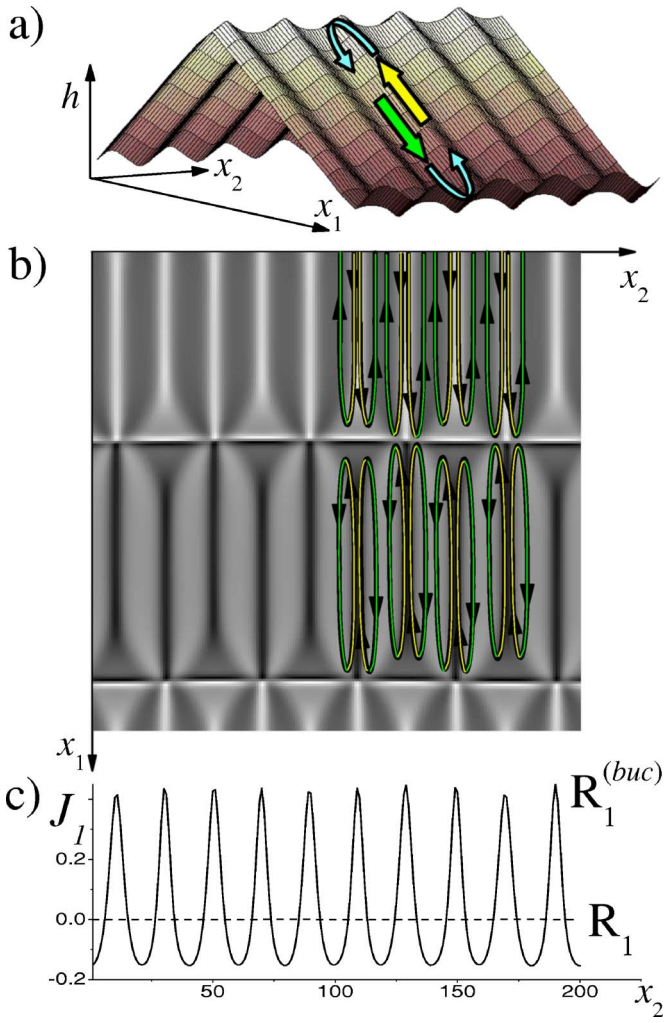

FIG. 9. (Color online) Persistent surface currents in the buckled rippled state, $R_1^{(\mathrm{buc})}$ in (a). In (c) we plot the current J_1 vs x_2 for a fixed x_1 which is away from tops and bottoms of the buckled ripples of the $R_1^{(\mathrm{buc})}$ state. The persistent current is downhill along the $R^{(\mathrm{buc})}$ facets and it is uphill along the edges between the facets. This yields a vortexlike behavior of the surface current: the current goes up the edges and circles back down along the facets. Overall surface current pattern has character of the vortex lattice depicted in (b), in which the currents are indicated atop the corresponding contour plot of $J_1(x_1,x_2)$. For comparison, in (c) we also plot (by the dashed line) the surface current J_1 for the ordinary rippled phase which approaches zero at long times when the facets become large.

$P(M_1,M_2,t)$ approaches a stable form having maxima at $\vec{M}$ values which are *off* the zeros of $\vec{J}^{(NE)}(\vec{M})$, see Fig. 8(c). Thus, the uncommon $R^{(\mathrm{buc})}$ state *does* exhibit the *slope distribution selection* although there are no stable zeros of $\vec{J}^{(NE)}(\vec{M})$. We find the $R^{(\mathrm{buc})}$ state to exhibit a *fast coarsening* seen in Fig. 8(a): the interface width $w\sim t^{\beta}$, with $\beta\approx 0.4$ close to the center of the $R^{(\mathrm{buc})}$ range in Fig. 3. We recall that a similar enhanced roughening is found in the *RhP* phase, in the proximity to the $R^{(\mathrm{buc})}$ domain in our kinetic phase diagram in Fig. 3 (see Fig. 5 and the discussions). Our simulations have revealed another interesting structural aspect of the buckled rippled state, documented in Fig. 10; this state is actually the buckled form of the rectangular rippled state. Indeed, from Fig. 10(b), one can see that the large scale morphology of the $R^{(\mathrm{buc})}$ state is that of the $R^{(\mathrm{rec})}$ state, with large huts and pits (inverted huts) forming a checkerboard structure. However, in contrast to the $R^{(\mathrm{rec})}$ state, the facets of the huts and pits of the $R^{(\mathrm{buc})}$ state are buckled, i.e., exhibit an additional modulation with a wavelength much smaller than the size of huts [see Fig. 10(b)]. This buckling deformation present in the $R^{(\mathrm{buc})}$ state disappears as the X point in phase diagram in Fig. 3 is approached, see Fig. 10(a). At the X point, the interface morphology is that of the $R^{(\mathrm{rec})}$ state.

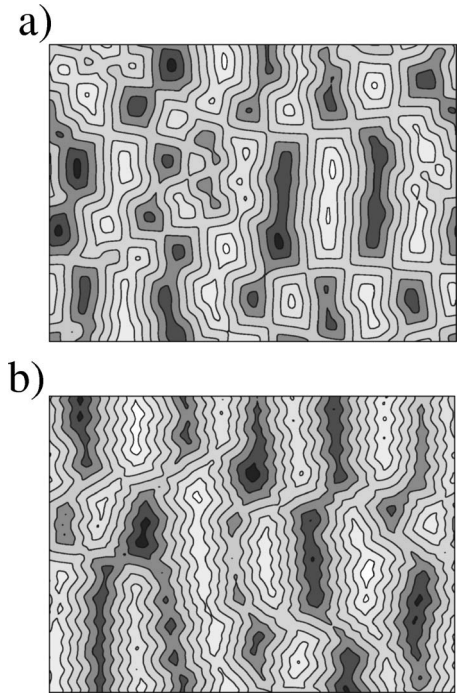

FIG. 10. (a) The interface contour plot obtained at the X point, exhibiting large huts and pits arranged as in the $R_1^{(\mathrm{rec})}$ state, which is just to the right of the X point, see Figs. 2 and 3. (b) The interface contour plot obtained in the $R_1^{(\mathrm{buc})}$ state, exhibiting large *buckled* huts and pits arranged as at the X point, which terminates the $R_1^{(\mathrm{buc})}$ range on its right-hand side, see Figs. 2 and 3. Thus, the $R_1^{(\mathrm{buc})}$ state is essentially the buckled form of the $R_1^{(\mathrm{rec})}$ state.

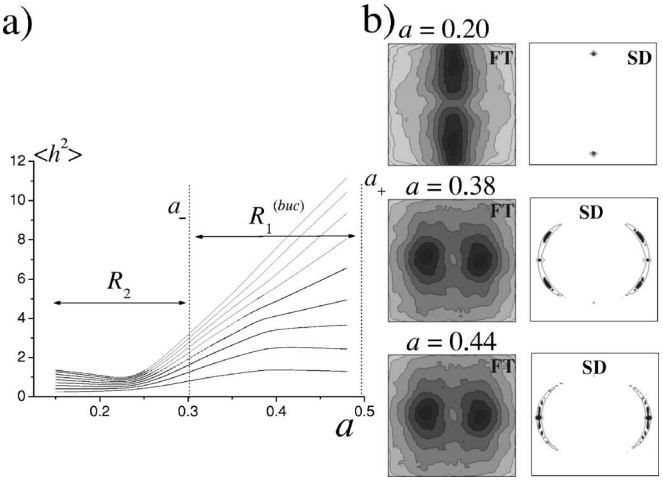

FIG. 11. (a) The square of the interfacial width $\langle h^2 \rangle$ vs the parameter a, given for several different times, across the transition from the rippled state R_2 (for $a < a_-$) to the buckled rippled state $R_1^{(\mathrm{buc})}$ (for $a > a_-$). This transition does not involve an intermediary state. (a) is obtained from numerous simulations done along the line $b = 1.1$ that goes from R_2 directly to $R_1^{(\mathrm{buc})}$ state. In (b), we give FT magnitudes and SDs found along this ripple rotation transition, for $a = 0.2$ (in the R_2 state), and for $a = 0.38$ and 0.44 (both within the $R_1^{(\mathrm{buc})}$ range). Note that FTs, i.e., near in-phase diffraction patterns of the $R_1^{(\mathrm{buc})}$ have just two peaks (like the R_1 pattern). Still, SDs, i.e., the out-of-phase diffraction patterns distinguish the $R_1^{(\mathrm{buc})}$ from the R_1 state. Overall, FTs and SDs of the $R_1^{(\mathrm{buc})}$ state here are similar to those of the intensely rough *RhP* state in Fig 5. However, note that the forms of SDs of $R_1^{(\mathrm{buc})}$ are closer or even indistinguishable from that of the R_1 state (see SD obtained at $a = 0.44$ here, still within the $R_1^{(\mathrm{buc})}$ range).

Structurally and, also, according to its position in the phase diagram in Figs. 2 and 3, the $R^{(\mathrm{buc})}$ state may also qualify to be the intermediary state seen in the erosion on Cu(110) and on Rh(110) surfaces [13]. This is documented by our simulations in Fig. 11, which depict details of the ripple rotation transition along a line going through the $R_1^{(\mathrm{buc})}$ state. Note that this figure is, overall, similar to Fig. 5(b), in which this transition goes through the intensely rough *RhP* state. Thus, by comparison with the near in-phase and out-of-phase diffraction data on Cu(110) and Rh(110) surfaces [13], we argue that these ripple rotation transitions go with the intervention of either intensely rough *RhP* (as in Fig. 5) or the $R_1^{(\mathrm{buc})}$ state (as in Fig. 11). In addition to the diffraction data, this statement is supported also by the fact that our *RhP* and $R_1^{(\mathrm{buc})}$ states both exhibit the experimentally seen enhanced coarsening with the interface width $\sim t^{0.4}$. In both cases, the experimentally seen hot-rippled phase corresponds to our R_2 phase. By decreasing the temperature T, the R_2 facets destabilize, and the interface transforms into the *RhP* or into the $R_1^{(\mathrm{buc})}$ state. At this point, it is illuminating to recall of our Fig. 2, and the fact that the R_2-to-*RhP* transition is a Hopf bifurcation in which R_2 facets destabilize and newborn *RhP* facets take over the interface morphology (see Sec. III and Appendix A). Microscopically, this facet destabilization with decreasing T can be caused by the Schwoebel barriers on the kinks on the terrace steps of the R_2 facets. These kinks are easily rounded by adatoms only at high enough T (so R_2 is stable there). With decreasing T, the R_2 facets destabilize due to the Schwoebel barriers, and the R_2 rippled state transforms into the *RhP* state. Likewise, a further decrease of temperature can destabilize the *RhP* facets and cause the transition into the fascinating $R_1^{(\mathrm{buc})}$ state that occurs in the situations in which *all* flat facets are unstable (see again our Fig. 2).

Based on this discussion of the microscopic effects underlying our phenomenological model, we argue that the interface morphology transformations seen on Cu(110) and Rh(110) surfaces [13] reflect one (or both) of the following two chains of far-from-equilibrium transitions:

Chain 1: with decreasing T,

$$R_2 \rightarrow RhP \rightarrow R_1^{(\mathrm{buc})}; \tag{4.3}$$

Chain 2: with decreasing T,

$$R_2 \rightarrow R_1^{(\mathrm{buc})}. \tag{4.4}$$

In both chains, the R_2 rippled state is the "hot rippled" state, and the $R_1^{(\mathrm{buc})}$ is the "cold rippled" state. Chain 1 has the intensely rough RhP as the intermediary state, manifested through the experimentally seen quartet slope distribution [see our Fig. 5(b)]. On the other hand, the Chain 2 in Eq. (4.4) does not involve an intermediary state at all. Nonetheless, this chain also reproduces the experimental fact that the quartet slope distribution is seen in an intermediary tempera-

ture range. This is documented by our simulations in Fig. 11 which gives the in-phase (FT) and out-of-phase (SD) diffraction patterns for Chain 2, with only R_2 and $R_1^{(\mathrm{buc})}$ states involved. Note that the SD of the $R_1^{(\mathrm{buc})}$ changes from the quartet form (occurring close to the R_2-to-$R_1^{(\mathrm{buc})}$ transition) to the R_1-like doublet form, occurring *even before* the $R_1^{(\mathrm{buc})}$-to-R_1 transition is reached. Thus, importantly, the fascinating buckled rippled state $R_1^{(\mathrm{buc})}$ reproduces the behaviors observed both in the intermediary (*RhP*-like) and in the ultimate low temperature (R_1-like) regime seen in the experiments [13].

Note added. The significance of our buckled rippled state for interpreting experimental data has been recognized also by the experimental workers, in the very recent study [20] on the ion erosion of Cu(110) surfaces. In addition, in the discussions of the rhomboidal pyramid state experimental properties, these authors have highlighted our phenomenology, in particular, the role of our phenomenological nonequilibrium current for understanding of the diffraction data behaviors. We also note that our phenomenological theory has motivated recent theoretical study [21]. Reference [21], as well as its corrected and clarified expositions [22], well illustrate tantalizing theoretical problems associated with calculating detailed analytic form of the nonequilibrium surface current starting from more microscopic considerations (bottom-to-top approach), even for the case of 1D interfaces. In the present phenomenological (top-to-bottom) approach, the 2D spatial symmetries of the nonequilibrium surface current (Sec. II), rather than its detailed analytic form, play the central role in predicting the rich multitude of conceptually and experimentally interesting interfacial states revealed by our theory.

ACKNOWLEDGMENTS

L.G. thanks DAAD for Grant No. A/02/15054 and the Max Plank Institute for the Physics of Complex Systems, Dresden, for hospitality.

APPENDIX A

To derive the stability conditions used in the discussions of Sec. III, we expand the interface profile $h(\vec{x},t)$ around a flat interface profile (facet), with the slope $\vec{M}_0$,

$$h(\vec{x},t) = \vec{M}_0\vec{x} + \delta h(\vec{x},t), \tag{A1}$$

or, in terms of the interface slope, $\vec{M}=\nabla h=\vec{M}_0+\vec{\nabla}\delta h=\vec{M}_0+\delta\vec{M}$. We will employ the expansion implied by Eq. (A1) to study the preferred facets $[\vec{J}^{NE}(\vec{M}_0)=\vec{0}]$ stability in our model Eq. (2.17). For this purpose, we first expand the nonequilibrium current $\vec{J}^{NE}(\vec{M})=[J_1^{NE}(M_1,M_2),J_2^{NE}(M_1,M_2)]$,

$$J_\alpha^{NE}(\vec{M}_0+\delta\vec{M}) = J_\alpha^{NE}(\vec{M}_0) + \sum_{\beta=1}^{2} \left.\frac{\partial J_\alpha^{NE}}{\partial M_\beta}\right|_{\vec{M}=\vec{M}_0} \delta M_\beta + \cdots \tag{A2}$$

Here, $\alpha=1,2$. By Eqs. (A2) and (2.1), and using $\partial\delta M_\beta/\partial x_\alpha=\partial\delta M_\alpha/\partial x_\beta=\partial^2\delta h/\partial x_\alpha\partial x_\beta$, we obtain

$$\frac{\partial}{\partial t}\delta h = -\sum_{\alpha=1}^{2}\sum_{\beta=1}^{2}\frac{1}{2}\left(\frac{\partial J_\alpha^{NE}}{\partial M_\beta}+\frac{\partial J_\beta^{NE}}{\partial M_\alpha}\right)_{\vec{M}=\vec{M}_0}\frac{\partial^2}{\partial x_\alpha\partial x_\beta}\delta h. \tag{A3}$$

Within the linear stability analysis, the nonlinear terms in $\delta h(\vec{x},t)$ are ignored in Eq. (A3). We also ignore the higher order derivative (curvature) terms that are subdominant in the long length scale (short wave vector) limit which governs the stability of large facets. It is assumed that these curvature terms [such as the surface diffusion term Eq. (2.3)] are stabilizing, i.e., that there are no short length scale instabilities. Thus, facet instability may emerge only at long length scales, from the terms exposed in Eq. (A3) which are purely due to the $\vec{J}^{NE}(\vec{M})$. Equation (A3) is solved by $\delta h(\vec{x},t)\sim\exp[\omega(q_1,q_2)t]\cdot\exp[iq_1x_1+iq_2x_2]$. Here, $\omega(q_1,q_2)$ is the dispersion relation,

$$\omega(q_1,q_2) = -(T_{11}q_1^2+2T_{12}q_1q_2+T_{22}q_2^2), \tag{A4}$$

with

$$T_{\alpha\beta}=T_{\beta\alpha}=-\frac{1}{2}\left(\frac{\partial J_\alpha^{NE}}{\partial M_\beta}+\frac{\partial J_\beta^{NE}}{\partial M_\alpha}\right). \tag{A5}$$

For a stable facet, $\omega(q_1,q_2)$ in Eq. (A4) must be negative for *any* (q_1, q_2), thus the matrix $T_{\alpha\beta}$ must be positively definite (PD). For our model Eq. (2.17), the stability matrix Eq. (A5) has the form

$$T_{11}(\vec{M}) = -(1+a)+3M_1^2+(b+c)M_2^2,$$

$$T_{12}(\vec{M}) = T_{21}(\vec{M}) = bM_1M_2,$$

$$T_{22}(\vec{M}) = -(1-a)+3M_2^2+(b-c)M_1^2. \tag{A6}$$

Let us analyze the stability of various types of zeros of $\vec{J}^{NE}(\vec{M})$ introduced in Sec. III.

Singlet $(M_1=M_2=0)$. For it, by Eqs. (A4)–(A6), we find the dispersion relation

$$\omega_{\mathrm{sin}}(\vec{q}) = q_1^2(1+a)+q_2^2(1-a). \tag{A7}$$

By Eq. (A7), for any a there are some values of $\vec{q}$ such that $\omega_{\mathrm{sin}}(\vec{q})>0$. Thus, the singlet is generally unstable.

R_1 *doublet* $(M_1\neq 0, M_2=0)$. By Eq. (3.1), this doublet exists only for $1+a>0$. Using Eqs. (3.1) and (A4)–(A6), we find the dispersion relation for the R_1 doublet,

$$\omega_{R_1}(\vec{q}) = -2q_1^2(1+a)-q_2^2(1+b-c)[a-a_+(b,c)]. \tag{A8}$$

Here, $a_+(b,c)$ is given by Eq. (3.4). By Eq. (A8), for $1+b-c>0$, the R_1 is unstable for $a<a_+(b,c)$ and stable for $a>a_+(b,c)$, as reported in Sec. III.

R_2 *doublet* $(M_1=0, M_2\neq 0)$. By Eq. (3.1), this doublet exists only for $1-a>0$. Using Eqs. (3.2) and (A4)–(A6), we find the dispersion relation for the R_2 doublet,

$$\omega_{R_2}(\vec{q}) = -2q_2^2(1-a) - q_1^2(1+b+c)[a_-(b,c)-a]. \tag{A9}$$

Here, $a_-(b,c)$ is given by Eq. (3.4). By Eq. (A9), for $1+b+c>0$, the R_2 is unstable for $a>a_-(b,c)$ and stable for $a<a_-(b,c)$, as anticipated in Sec. III.

Quartet ($M_1\neq 0, M_2\neq 0$). Here, M_1 and M_2 are as in Eq. (3.3), which can be used to show that the quartet zero exists only between the lines a_+ and a_- in Fig. 3. Using Eqs. (3.3) and (A4)–(A6), we find the dispersion relation for the quartet

$$\omega_{quart}(\vec{q}) = -2q_1^2M_1^2 - 2q_2^2M_2^2 - 4bq_1q_2M_1M_2. \tag{A10}$$

By denoting here $Q_1=q_1M_1$, and $Q_2=q_2M_2$, Eq. (A10) reduces to

$$\omega_{quart}(\vec{Q}) = -2Q_1^2\left[\left(\frac{Q_2}{Q_1}+b\right)^2 + 1 - b^2\right], \tag{A11}$$

showing that the quartet is stable for $b<1$ and a between a_+ and a_-, as reported in Sec. III. We recall that in this range the *RhP* interfacial structure develops (see Secs. III and IV). On the other hand, by Eq. (A11), the quartet becomes unstable for $b>1$. By the above discussions, for b in the range $1<b<b_X=\sqrt{1+c^2}$ and a between a_+ and a_-, *all* zeros of $\vec{J}^{NE}(\vec{M})$ are unstable. In this range (notably existing only if $c\neq 0$), the interface cannot develop large flat facets corresponding to any of the zeros of $\vec{J}^{NE}(\vec{M})$. Rather, therein, the unusual buckled rippled state develops, with an interface morphology carrying nonzero surface currents (see Sec. IV and Fig. 9). This state disappears for $c\to 0$ whence the dynamics becomes governed by an effective free energy, yielding the current $\vec{J}^{NE}(\vec{M})=-\partial U/\partial\vec{M}$ [see Eq. (2.12a)], and thus by Eq. (A5), $T_{\alpha\beta}=\partial^2 U/\partial M_\alpha\partial M_\beta$. The selected facet then corresponds to the absolute minimum of $U(\vec{M})$, which is assured to be stable, i.e., its Hessian matrix $T_{\alpha\beta}$ must be PD. Thus, for the case $c=0$, the existence of F_{eff} prohibits the situation with all zeros of $\vec{J}^{NE}(\vec{M})$ being unstable.

APPENDIX B

In this appendix, we prove our theorem Eq. (3.10) on the static edges between two preferred facets with the slopes $\vec{M}_A$ and $\vec{M}_B$, and apply it to derive our Eq. (3.9). Along an edge the two facets intersect, so $\vec{M}_A\cdot\vec{x}=\vec{M}_B\cdot\vec{x}$ with $\vec{x}=|\vec{x}|\hat{e}$ where $\hat{e}$ is the unit vector along the edge. Thus, $\vec{M}_A\cdot\hat{e}=\vec{M}_B\cdot\hat{e}$, see Fig. 12. This equation actually determines $\hat{e}$ for a given $\vec{M}_A$ and $\vec{M}_B$. Let us denote by $\hat{t}$ the unit vector perpendicular to $\hat{e}$, $\hat{t}\cdot\hat{e}=0$, and let us employ the edge based Cartesian coordinate system associated with unit vectors $\hat{e}$ and $\hat{t}$. Thus, we change the base-plane coordinates as $\vec{x}=x_1\hat{i}_1+x_2\hat{i}_2=x_L\hat{e}+x_T\hat{t}$. Here, (x_1,x_2) are the original coordinates (as in Sec. II), whereas x_L and x_T, are, respectively, the longitudinal (along the edge) and perpendicular (to the edge) coordinates. It will be convenient to express the vectors $\vec{M}$ and $\vec{J}^{NE}$ using these edge based coordinate system, via

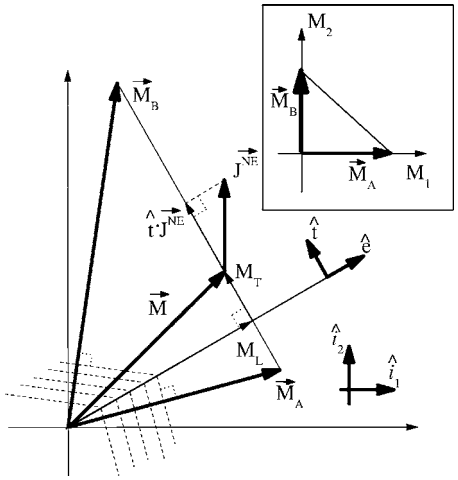

FIG. 12. The figure aids the derivation of Eq. (3.10); see Appendix B text. The inset depicts the integration path used in Eq. (3.10) to derive Eq. (3.9).

$$\vec{M} = M_1\hat{i}_1 + M_2\hat{i}_2 = M_L\hat{e} + M_T\hat{t},$$

$$\vec{J}^{(NE)} = J_1^{(NE)}\hat{i}_1 + J_2^{(NE)}\hat{i}_2 = J_L^{(NE)}\hat{e} + J_T^{(NE)}\hat{t}, \tag{B1}$$

see Fig. 12. This change of coordinates is a rotation, preserving the form of the 2D divergence,

$$\vec{\nabla}\cdot\vec{J}^{(NE)} = \frac{\partial J_1^{(NE)}}{\partial x_1} + \frac{\partial J_2^{(NE)}}{\partial x_2} = \frac{\partial J_L^{(NE)}}{\partial x_L} + \frac{\partial J_T^{(NE)}}{\partial x_T}. \tag{B2}$$

For the infinitely long edge, the interface profile has the form

$$h(\vec{x}) = x_L M_e + \psi(x_T), \tag{B3}$$

see the contour lines in Fig. 12. The corresponding slope vector components are

$$M_L = \frac{\partial h}{\partial x_L} = M_e = \text{const},$$

$$M_T = \frac{\partial h}{\partial x_T} = M_T(x_T) = \frac{d\psi(x_T)}{dx_T}, \tag{B4}$$

i.e., $M_L=\vec{M}\cdot\hat{e}$ is just a constant, whereas $M_T(x_T)=\vec{M}\cdot\hat{t}$ is a function of x_T only. An edge is analogous to a domain wall in a magnetic system, with the slope

$$\vec{M}(x_T) = M_e\hat{e} + M_T(x_T)\hat{t}, \tag{B5}$$

approaching $\vec{M}_A$ for $x_T\to-\infty$, and $\vec{M}_B$ for $x_T\to+\infty$. To discuss the form of $M_T(x_T)$, note that $\vec{J}^{NE}(\vec{M})$, by Eq. (B5), depends on x_T only. Thus, by Eq. (B2),

$$\vec{\nabla}\vec{J}^{NE} = \frac{dJ_T^{NE}}{dx_T} = \frac{d}{dx_T}(\hat{t}\cdot\vec{J}^{NE}(\vec{M})). \tag{B6}$$

For the static edge, $\partial h/\partial t=0$, and by Eqs. (2.17), (B4), and (B6), we find

$$0 = \frac{d}{dx_T}(\hat{t}\cdot\vec{J}^{NE}) - k_T\left(\frac{d}{dx_T}\right)^4 \psi(x_T), \tag{B7}$$

where k_T is a linear combination of the constants $k_{\alpha\beta}$ in Eq. (2.17a). By Eqs. (B7) and (B4), one can easily see that

$$-\hat{t}\cdot\vec{J}^{NE}(\vec{M}) - k_T\frac{d^2M_T(x_T)}{dx_T^2} = \text{const} = 0. \tag{B8}$$

The const in (B8) is zero as for $x_\perp \to \pm\infty$ the preferred slopes $\vec{M}_A$ and $\vec{M}_B$ are asymptotically reached and the $\vec{J}^{NE}\to 0$. Equation (B8) is isomorphic to that of the Newtonian dynamics of a particle with the mass k_T and the position $M_T(x_T)$ versus time x_T, moving under the force $\sim\hat{t}\cdot\vec{J}^{NE}(\vec{M})$. The particle's kinetic energy $\sim(dM_T/dx_T)^2$ approaches zero in the limits $x_T\to-\infty$ and $x_T\to+\infty$, in which $M_T\to(\vec{M}_A)_T$ and $M_T \to(\vec{M}_B)_T$, respectively, see Fig. 12. Thus, the total work of the force $\sim\hat{t}\cdot\vec{J}^{NE}(\vec{M})$ along this displacement is zero,

$$\int_{(\vec{M}_A)_T}^{(\vec{M}_B)_T} dM_T(\hat{t}\cdot\vec{J}(\vec{M})) = 0. \tag{B9}$$

By Eq. (B5), one can see that Eq. (B9) is equivalent to Eq. (3.10), with the integration path in the M space being the straight line segment connecting the tips of facet vectors $\vec{M}_A$ and $\vec{M}_B$. This completes our proof of the theorem in Eq. (3.10). Let us apply it to the static edge between one of R_1 facets, with the slope vector $\vec{M}_A=(\sqrt{1+a},0)$, and one of the R_2 facets, with the slope vector $\vec{M}_B=(0,\sqrt{1-a})$, see Eqs. (3.1) and (3.2), and Fig. 12 inset. By performing the line integral in Eq. (3.10) along the straight line segment joining the tips of $\vec{M}_A$ with $\vec{M}_B$ [see Fig. 12 (inset)], for $\vec{J}^{NE}(\vec{M})$ in Eq. (2.17b), we find that

$$\int_{\vec{M}_A}^{\vec{M}_B} d\vec{M}\cdot\vec{J}^{NE}(\vec{M}) = -a + \frac{1}{6}c(1-a^2) = 0. \tag{B10}$$

Solving the equation Eq. (B10) for a yields the critical value, a_{cr} stated in Eq. (3.9). Of the two solutions of Eq. (B10), only the one with $|a|<1$ is physical (see the form of $\vec{M}_A$ and $\vec{M}_B$ here).

[1] D. Moldovan and L. Golubovic, Phys. Rev. E **61**, 6190 (2000).
[2] M. Siegert, Phys. Rev. Lett. **81**, 5481 (1998).
[3] L. Golubovic, A. Levandovsky, and D. Moldovan, Phys. Rev. Lett. **89**, 266104 (2002).
[4] A. Levandovsky and L. Golubovic, Phys. Rev. B **69**, 241402(R) (2004).
[5] See, J. Krug, Adv. Phys. **46**, 139 (1997); Physica A **313**, 47 (2002).
[6] J. Villain, J. Phys. I **1**, 19 (1991).
[7] T. Michely, M. Kalff, G. Comsa, M. Strobel, and K.-H. Heinig, Phys. Rev. Lett. **86**, 2589 (2001); J.-K. Zuo and J. F. Wendelken, *ibid.* **78**, 2791 (1997).
[8] Jacques G. Amar, Phys. Rev. B **60**, R11 317 (1999).
[9] F. Buatier de Mongeot, G. Costantini, C. Boragno, and U. Valbusa, Phys. Rev. Lett. **84**, 2445 (2000). This study was the first one to report the ripple rotation transition on a (110) crystal surface, for the case of the Ag(110) surface (epitaxial growth), and to reveal an intermediary state intervening in the transition. F. Hontinfinde and R. Ferrando, Phys. Rev. B **63**, 121403 (2001), pursued a KMC investigation of this phenomenon.
[10] G. Constantini, S. Rusponi, F. Bautier de Mongeot, C. Boragno, and U. Valbusa, J. Phys.: Condens. Matter **13**, 5875 (2001).
[11] M. Albrecht, H. Fritzsche and U. Gradmann, Surf. Sci. **294**, 1 (1993).
[12] K. J. Caspersen, A. R. Layson, C. R. Stoldt, V. Fournee, P. A. Thiel, and J. W. Evans, Phys. Rev. B **65**, 193407 (2002).
[13] A. Molle, F. B. de Mongeot, A. Molinari, F. Xiaerding, C. Boragno, and U. Valbusa, Phys. Rev. Lett. **93**, 256103 (2004); and Ref. [20]. These studies have revealed our rhomboidal pyramid state to be present in the erosion on Cu(110) and Rh(100) surfaces. See also F. Buatier de Mongeot, A. Toma, A. Molle, S. Lizzit, L. Petaccia, and A. Baraldi, *ibid.* **97**, 056103 (2006).
[14] F. Buatier de Mongeot, W. Zhu, A. Molle, R. Buzio, C. Boragno, U. Valbusa, E. G. Wang, and Z. Zhang, Phys. Rev. Lett. **91**, 016102 (2003).
[15] J. Toner and D. R. Nelson, Phys. Rev. B **23**, 316 (1981).
[16] A. Levandovsky and L. Golubovic (unpublished).
[17] Over the time scales in which $\vec{M}$ still approaches its preferred value, the dynamics can be modeled by Eqs. (2.1) and (2.2) with $\vec{J}^{NE}(\vec{M})\sim 1/|M|^{\eta-1}$, and $-\vec{\nabla}J^{SD}\sim-(-\nabla^2)^m h$, yielding the coarsening exponents $n=1/2m$, $\beta=(2m+\eta-2)/2m\eta$; see, L. Golubovic, Phys. Rev. Lett. **78**, 90 (1997). For $m\approx 6$, $\eta\approx 3.7$, these results reproduce the experimental values $n\approx 0.09$, $\beta\approx 0.31$ seen in the ion erosion of Cu(110) in Ref. [20]. We also note that the non-standard surface relaxation, with $m\geqslant 3$, i. e., $n=1/2m\leqslant 1/6\approx 0.16$ have been seen before in experiments [see J. A. Stroscio, D. T. Pierce, M. D. Stiles, A. Zangwill, and L. M. Sander, Phys. Rev. Lett. **75**, 4246 (1995); and Ref. [12]].
[18] A. Levandovsky, L. Golubovic, and D. Moldovan, in *Modeling of Morphological Evolution at Surfaces and Interfaces*, edited by J. Evans, C. Orme, M. Asta, and Z. Zhang, MRS Symposia Proceedings No. 859E (Materials Research Society, Pittsburgh, 2005).
[19] See, e.g., H. Haken, *Synegetics* (Springer-Verlag, Berlin, 1978).
[20] A. Molle, F. Buatier de Mongeot, A. Molinari, C. Boragno, and U. Valbusa, Phys. Rev. B **73**, 155418 (2006).
[21] M. Li and J. W. Evans, Phys. Rev. Lett. **95**, 256101 (2005).
[22] M. Li and J. W. Evans, Phys. Rev. Lett. **96**, 079902(E) (2006); Phys. Rev. B **73**, 125434 (2006).